4

Modelling the pre-industrial state

4.1 Introduction

The biogeochemical processes previously outlined delineate what is essentially a framework for representing the global (oceanic) carbon cycle. However, before SUE can be employed to test potential mechanisms behind the observed glacial-interglacial variability in the concentration of atmospheric CO_2, model ocean structure and circulation must be prescribed. Furthermore, the existence of a number of unconstrained parameter values within certain process parameterizations dictates that a degree of model 'optimization' must be carried out. The end-product of this optimization will be a steady-state representation of the modern (pre-industrial) carbon cycle which can be used to critically evaluate the model's performance against observational data.

Parameter optimization and model evaluation should ideally be undertaken within a rigorous statistical framework, with indicators of 'goodness of fit' defined and utilized in order to achieve some quantitatively optimal model solution. System characteristics such as atmospheric composition, fields of physical and chemical ocean properties, areal distributions of biological production and sediment composition are all important indicators of system operation and therefore need to be considered in constructing any hypothetical 'goodness of fit' statistic. However, in order to achieve this, weightings of relative importance to the overall system response of the carbon cycle must be assigned to all these individual components. Unfortunately it is not possible in the context of this present study for such an approach to be undertaken since these assignments cannot be made unobjectively. Furthermore, with the exception of a few predominantly global values such as the concentration of atmospheric CO_2 and its isotopic signature, there is a serious scale mismatch between the descriptors of model state and observational data. While model ocean properties are regional in character, typically representing zonal or even entire basin averages, much of available observational data is in the form of point measurements, for which system characteristics such as biological productivity (and to a lesser extent, sediment composition) are extremely patchy in their global coverage. Instead, a 'reasonable' model state is objectively judged through consideration of a basket of apparently important system characteristics. In any event, the modern ocean carbon cycle is likely to be far from steady state, even prior to the advent of the Industrial Revolution. The validity of an exact simile of the pre-industrial system obtained with a steady state model is thus questionable, particularly for subsequent application to long-term change.

4.2 Ocean structure and circulation

Historically, substantial progress in our understanding of the potential causes behind the relatively low concentration of atmospheric CO_2 (xCO_2) observed to have occurred during the Last Glacial Maximum (LGM) has been made with the use of global carbon cycle models where the representation of the world ocean is highly simplified. In some of the earliest of these models the ocean was partitioned into only two or three homogeneous volumes or 'boxes' with a prescribed ocean circulation (e.g., *Knox and McElroy* [1984], *Sarmiento and Toggweiler* [1984], *Siegenthaler and Wenk* [1984]), soon followed by slightly more complex 'multi-box' models utilizing up to a few dozen boxes (e.g., *Broecker and Peng* [1986], *Keir* [1988]). Despite their apparent oceanographic naivety they are advantaged by relative ease of interpretation and numerical efficiency [*Joos et al.*, 1997; *Sarmiento et al.*, 1988; *Siegenthaler and Joos*, 1992] which has led to them playing a central role in the development of many of the mechanisms for glacial-interglacial xCO_2 changes proposed to date. However, a number of problems in representing the ocean carbon cycle arise, particularly as a result of the low vertical and horizontal resolution inherent in ocean structures comprising no more than a few dozen distinct elements;

- The remineralization of particulate organic matter (POM), $CaCO_3$, and opal within the water column are unlikely to be adequately resolved. Vertical adjacency between boxes lying at the surface (where nutrients may be limiting to biological productivity) and at intermediate depths (where most POM remineralization and nutrient release occurs) can lead to 'nutrient trapping' problems (see 4.3.4).
- The scavenging of Fe from the water column is similarly likely to suffer from low vertical resolution. Low horizontal resolution may also distort the system, particularly where regions receiving high aeolian Fe supply incorrectly adjoin regions of low aeolian supply rather than being separated by a zone where scavenging can restrict Fe transfer.
- With relatively low (mainly horizontal) resolution model validation attempted between spatially-aggregated model descriptors and point observations taken from paleoceanographic sediment cores becomes difficult.
- Failure to resolve important regions of CO_2 ocean-atmosphere exchange (such as strong net out-gassing from equatorial up-welling zones) may distort the dynamical response of xCO_2 to perturbations, even if model tuning allows for a realistic pre-industrial value to be simulated at steady-state.
- Circulation fields generated by tuning to a single tracer such as radiocarbon (natural or bomb) may be in error when applied to other tracers [*Joos et al.*, 1997; *Kurz and Maier-Reimer*, 1993; *Siegenthaler and Joos*, 1992].

Increasing the number of boxes beyond a few dozen in an attempt to alleviate these problems makes it difficult to construct a self-consistent and realistic ocean circulation. An alternative way of increasing vertical resolution is to use a diffusive box model [*Oeschger et al.*, 1975; *Shaffer*, 1989, 1993, 1996; *Shaffer and Sarmiento*, 1995]. However, where there is no analytical solution, this improvement is achieved at the expense of computational efficiency and issues related to horizontal resolution still remain. A final possible trick is to sub-divide vertically and/or horizontally boxes in an existing box model whilst retaining the original advective field [*Klepper et al.*, 1994].

In contrast to box models, Ocean General Circulation Models (OGCMs) represent the global ocean on a three-dimensional grid, with a typical horizontal resolution of order 3° and with upwards of 15-30 separate vertical levels resolved. Ocean circulation is calculated by consideration of forces generated through surface wind stress and ocean density contrasts (driven by heat and salinity gradients) [*McGuffie and Henderson-Seller*, 1996], with surface boundary conditions prescribed from observations or calculated through coupling with an (Atmospheric) General Circulation Model (GCM or AGCM). Although their grid spacing enables most major ocean biogeochemical provinces to be adequately resolved, the shear number of cells in the 3D structure results in a considerable computation requirement, even when run 'off-line' (i.e., utilizing a pre-calculated circulation [*Bacastow and Maier-Reimer*, 1990]). The simulation of entire glacial-interglacial cycles is therefore currently beyond the practical application of most OGCMs, particularly where extensive sensitivity analyses might be required. In addition, despite having an apparently strong semblance of reality about them OGCMs are far from perfect, for instance often exhibiting serious deficiencies in equatorial circulation which are highlighted when biogeochemical cycling is incorporated [*Najjar et al.*, 1992]. Although such problems can be corrected with the use of a sufficiently fine grid spacing [*Aumont et al.*, 1999], this adds further to the computational costs of running the model.

There is, however, something of a "third way". Zonally-averaged OGCMs (also known as '2D' or '2.5D' models, but referred to as 'ZOGCM's hereafter) divide the ocean meridionally into a number of latitudinal bands with a typical resolution of 5-15°. The ocean is therefore zonally averaged although each basin is represented separately. The number of vertical levels is comparable to that of full (3D) OGCMs. As with OGCMs, ocean circulation is calculated from basic fluid physics, albeit in a more highly parameterized form [*Wright and Stocker*, 1992]. While they cannot represent sub-zonal features such as boundary currents they are successful in reproducing the global and basin-scale features such as the Atlantic thermohaline circulation [*Hovine and Fichefet*, 1994; *Wright and Stocker*, 1992]. Indeed, simple single-basin models have been successfully employed in investigating modes of variability in overturning circulation [*Drbohlav and Jin*, 1998; *Yang and Huang*, 1996; *Yang and Neelin*, 1993]. The relatively short integration times of ZOGCMs achieved through zonal averaging (compared to that possible with a true 3D grid) together with their ability to produce an interactive ocean circulation (as opposed to the fixed prescribed circulation of box models) has made them ideal candidates for integrating into complete Earth System Models (ESMs) [*Ganopolski et al.*, 1998a,b; *Sakai and Peltier*, 1997, 1998].

The flexibility in physical ocean structure enabled by SUE allows for implementation of a ZOGCM-type configuration as an alternative to a simple multi-box model format. While a number of different zonally-averaged global ocean circulation models have been developed (e.g., *Fichefet et al.* [1994], *Hovine and Fichefet* [1994], *Sakai and Peltier* [1996, 1997, 1998]), as an initial step the Bern 2D model is utilized [*Stocker et al.*, 1992; *Stocker and Wright*, 1991a, 1996; *Wright and Stocker*, 1991, 1992]. This has an ocean structure slightly simpler than possible alternatives, consisting of three zonally-averaged ocean basins (Atlantic, Indian, and Pacific) with a variable meridional resolution of between 7.5 and 15.0° (Figure 4-1). The three basins are linked by a Southern Ocean component with meridional but no zonal structure. 14 ocean levels are considered in the vertical. It also has the advantage of arguably the longest application pedigree, having been previously used in contexts such as ocean thermohaline circulation sensitivity [*Stocker and Wright*, 1991b], anthropogenic CO_2 uptake [*Stocker et al.*, 1994] and future feedbacks [*Joos et al.*, 1999], deglacial changes in the ocean ^{14}C reservoir [*Stocker and Wright*, 1996] and factors affecting surface ocean $\delta^{13}C$ distributions [*Lynch-Stieglitz et al.*, 1995]. Of obvious relevance to this present study is the fact that with the addition of a comprehensive carbon cycle [*Marchal et al.*, 1998b] the Bern 2D model has been previously employed in exploring the influence of changes in ocean circulation on xCO_2 [*Marchal et al.*, 1998a,b, 1999].

Although ocean circulation in the version of the Bern 2D model considered for application in SUE is annual [*Stocker and Wright*, 1996], important variability in the actual ocean system occurs seasonally. In particular, physical properties such as sea ice extent and mixed layer depth change markedly over the course of the year at high latitudes, leading to profound biogeochemical changes. The relatively sensitivity of CO_2 fugacity (fCO_2) with respect to ocean-atmosphere exchange CO_2 in a surface ocean layer thickness of ~50 m dictates that for numerical stability, carbon transfer across the air-sea interface in SUE must operate with a time step of order one month as opposed to annually. Taking advantage of this, an extremely crude pseudo-seasonality for high latitude processes is introduced in conjunction with a calculated annual insolation cycle (Appendix II). Firstly, fractional sea ice coverage is varied at the monthly time step according to relative changes in insolation levels. Although the cryosphere actually tends to lag changes insolation maximum sea ice extent is assumed to coincide with the winter insolation minimum, while minimum sea ice extent coincides with the summer maximum

$$A^{\text{ice}}_{(t)} = A^{\text{ice}}_{\text{min}} \cdot \left(A^{\text{ice}}_{\text{max}} - A^{\text{ice}}_{\text{min}} \right) \cdot \frac{I_{\text{max}} - I_{(t)}}{I_{\text{max}} - I_{\text{min}}} \qquad (4\text{-}1)$$

where for each grid point, $A^{\text{ice}}_{(t)}$ is the sea ice-covered area at time t, $A^{\text{ice}}_{\text{max}}$ and $A^{\text{ice}}_{\text{min}}$ are the maximum and minimum sea ice-covered areas, respectively, with insolation (I) variables, similarly designated. Secondly, a 'winter' season is defined (used subsequently in the representation of seasonal convection – see 4.2.3.1) at a particular grid point on the basis of mean monthly insolation falling below a prescribed threshold. This threshold is arbitrarily set at a value of $I = 0.225$, giving a plausible 'winter' season of length 4-6 months south of ~55°S.

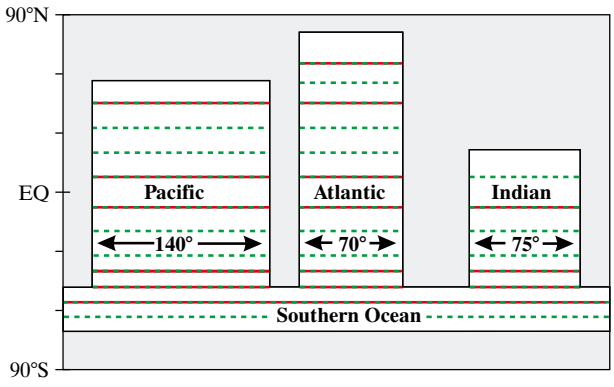

Figure 4-1 Configuration of the grid point regions in SUE1608 together with the location of boundaries of the parent Bern 2D ZOGCM [*Stocker and Wright*, 1996]. Meridional boundaries in SUE1608 are shown in red, whilst those of the Bern 2D model in green.

For carbon cycle work, OGCMs are typically run in an 'off-line' mode where a previously calculated advective field is imposed on the ocean biogeochemistry [*Archer et al.*, 2000; *Bacastow and Maier-Reimer*, 1990]. Such a configuration could virtually be considered a box model, albeit one with a huge number of boxes (in the range 10^3-10^5). By defining a structure of meta cells in the ocean, each of which encompassing multiple cells of the original ocean model, and by integrating fluxes across each of the meta cells boundaries, a new model structure can be obtained [*Michel et al.*, 1995]. While this 'child' structure will be characterized by lower vertical and/or horizontal resolution, ocean circulation should retain the basic characteristics of the 'parent' OGCM. Depending on to what extent resolution is degraded, a hierarchy of child models is possible based upon the same parent.

A new 'pseudo-box' model of the ocean carbon cycle for use over glacial-interglacial time scales is presented here (shown schematically in Figure 4-2) based upon the ocean configuration and circulation of the Bern 2D ZOGCM [*Stocker and Wright*, 1996]. Since its physical structure comprises 16 grid points horizontally with 8 levels in the vertical, it will hereafter be referred to as "SUE1608".

4.2.1 Derivation of basic ocean structure

Ocean zonation results in a relatively uncomplicated model circulation field, with mass flow often in the same direction across a series of adjacent cell boundaries. This allows horizontal and vertical resolution to be degraded without any serious distortion of the overall circulation pattern. Grid points in the Bern 2D model are therefore amalgamated in

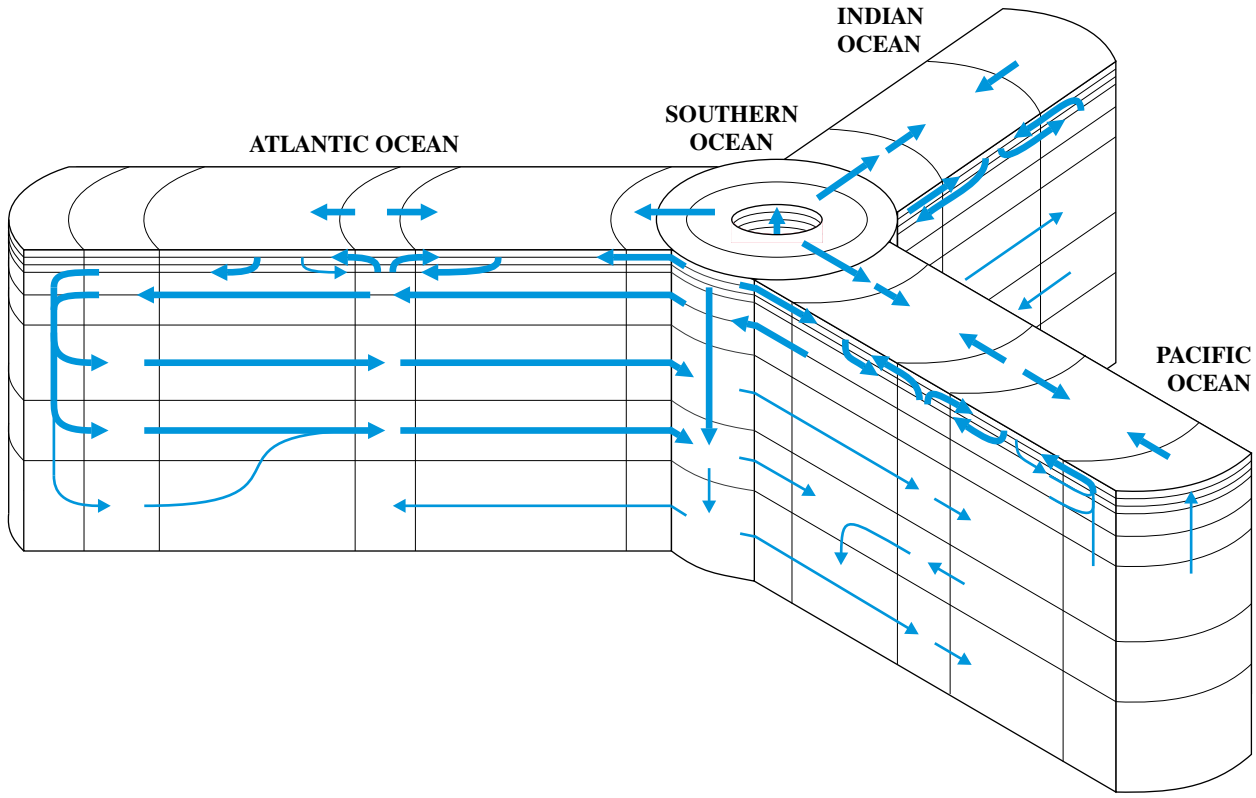

Figure 4-2 Ocean structure and schematic advective field of 'SUE1608'.

such a way that primary biogeochemically distinct surface regions and water masses are retained, the aim being to produce a minimum 'reasonable' representation of the ocean within the context of glacial-interglacial change and within constraints dictated by computational practicalities.

Taking the Bern 2D model, latitudinal boundaries are removed as indicated in Figure 4-1. A single grid point now represents the entire mid-latitude gyre zone (one for each hemisphere and for each of the ocean basins), the sub-polar zone of the Atlantic is enlarged, and both zones lying south of 50°S (the boundary which can be crudely taken to represent the location of the Antarctic Polar Front) in the Southern Ocean are merged. Since the spatial and seasonal complexity in Indian Ocean circulation north of 7.5°S is not reproduced in the parent model, both these regions are also amalgamated with little loss in realism. This leaves a total of 16 geographically distinct ocean regions.

In the vertical, the 50 m near-surface resolution is retained down as far as 150m, with layers amalgamated thereafter according to the apparent delineation of major water masses. A total of 8 vertical levels with lower boundaries at depths of 50, 100, 150, 500, 1000, 2500, 3500, and 4000 m are therefore retained. The overall reduction in the total number of cells by factor ~3 in SUE1608 results in a more than doubling in computational speed compared to that of the Bern 2D parent.

4.2.2 Physical boundary conditions

Physical ocean configuration in the Bern 2D model is highly idealized, assuming uniform zonal widths for each basin and with the longitudinal locations of the basin boundaries not specified in absolute terms [*Stocker and Wright*, 1996]. Regions associated with each model grid point are therefore prescribed as shown in Figure 4-3 for the purpose of deriving surface forcing data from observational fields. Forcing values for each region are then

$$b^{x}_{\text{mean}} = \frac{\sum_{\text{lat}}\sum_{\text{lon}} H\left(D_{(\text{lat,lon})}\right)\cdot A_{(\text{lat,lon})}\cdot b^{x}_{(\text{lat,lon})}}{\sum_{\text{lat}}\sum_{\text{lon}} H\left(D_{(\text{lat,lon})}\right)\cdot A_{(\text{lat,lon})}} \qquad (4\text{-}2)$$

where D is the depth of the ocean floor (m) taken from *ETOPO5* [1988], A is the ocean surface area associated with each ETOPO5 $5' \times 5'$ pixel, H is the Heavyside operator (acting to exclude terrestrial regions as defined by topography lying above sea level) and $b^{x}_{(\text{lat,lon})}$ is the observed value of surface property x. The physical boundary condition fields utilized are;

- Sea-surface temperature (SST) - from *Levitus et al.* [1994c] (taken at 30 m depth).
- Sea-surface salinity (SSS) - from *Levitus et al.* [1994b] (taken at 30 m depth), but modified in the southernmost grid cell (i.e., south of 55°S) to enable observed

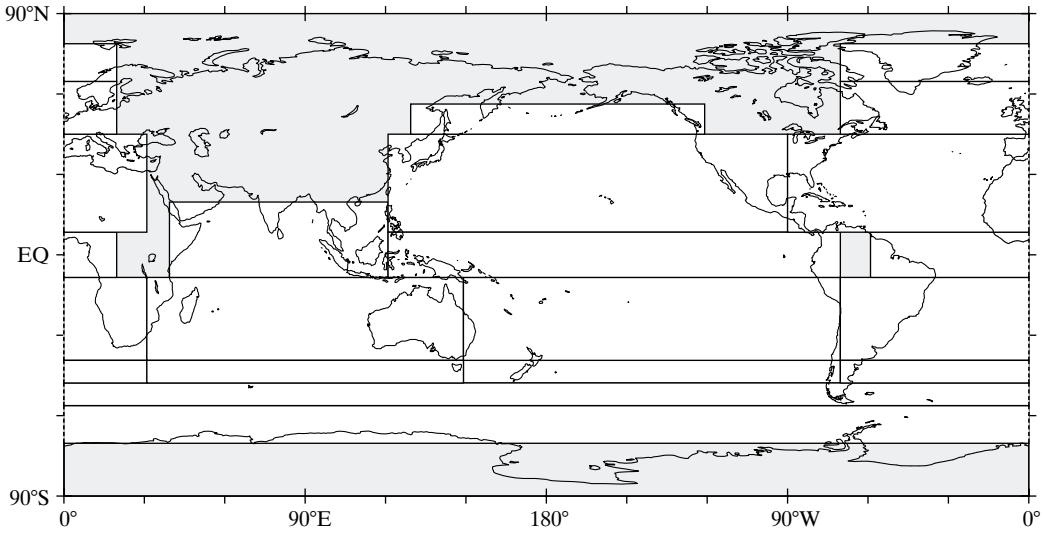

Figure 4-3 Prescribed ocean grid point regions in SUE1608.

deep-water values to be reproduced in that region [*Stocker and Wright*, 1996].

- Annual wind speed - calculated as an annual mean from individual monthly values [*Trenberth et al.*, 1989].
- Maximum sea ice coverage - set equal to the maximum (winter) monthly value [*CLIMAP*, 1984].
- Minimum sea ice coverage - set equal to the minimum (summer) monthly value [*CLIMAP*, 1984].
- Maximum mixed-layer depth - set equal to the deepest mean monthly depth of the mixed layer [*Levitus et al.*, 1994b,c].

Insolation is treated slightly differently, taking a value for each grid point region simply calculated at its mid-latitude (see Appendix II).

Unlike the meridional boundaries of each surface forcing region which have an exact correspondence with the physical ocean model, the longitudinal boundaries of the forcing regions are constrained in order to approximate actual basin topology. They therefore differ from those in the physical model. The resulting difference in area between the forcing and physical model grid point regions is a potential source of bias in terms of magnitude of mean global boundary conditions. However, even for surface properties that vary strongly with latitude such as SST, the area-weighted global mean surface temperature of the model is not significantly different (~0.1°C) from that derived directly from observations [*Levitus et al.*, 1994c].

4.2.3 Derivation of basic ocean circulation

Ocean circulation is taken from the modern (pre-industrial) annual velocity field of the Bern 2D ZOGCM [*Marchal et al.*, 1998a]. Meridional and vertical components of velocity are converted to an equivalent mass flow before any cell amalgamation takes place. Both net advection and exchange (mixing) across each of the internal physical ocean boundaries in SUE1608 are calculated.

4.2.3.1 Convective processes

While the derivation of a new advective field is relatively straightforward, the limited spatial and temporal resolution of the Bern 2D model makes representation of non-advective circulation, such as (high latitude) convective processes extremely problematic. While convection in the actual ocean is a seasonal process operating on relatively fine spatial scales and occurring heterogeneously within a zonal region, in contrast, the Bern 2D model has no true seasonality and is characterized by extensive homogeneous zonal regions. SUE1608 suffers from an additional deficiency with regard to convective processes in that it lacks any thermodynamic consideration of sea ice formation. As a result, application of commonly-used algorithms for convective adjustment in regions of water column density instability (identified according to the equation of state polynomial approximation of *Winton and Sarachik* [1993]) produces an overly-ventilated and homogenized deep high latitude ocean [*Stocker and Wright*, 1996]. This situation is exacerbated if Levitus SSSs [*Levitus et al.*, 1994b] are adjusted in order to produce more realistic deep-water salinities [*Stocker and Wright*, 1996]. Where water column instabilities do not extend all the way down to the ocean floor, pronounced hiatuses in temperature (T), salinity (S), and nutrient distributions can arise. Three highly parameterized processes are therefore introduced into the model in an attempt to capture (to a first order) observed high latitude behaviour – one for each of; seasonal mixed layer deepening, the formation of deep water masses characterized by low temperature, high salinity, and high dissolved O_2 concentrations, and generally enhanced vertical

mixing in the water column arising through convective and other sub-grid scale processes.

Mixed-layer dynamics

There is a pronounced seasonal cycle apparent at high latitudes. Summer months are characterized by high insolation levels and a stratification of the surface ocean, providing physical conditions suitable for rapid phytoplankton growth. In contrast, during winter months biological activity is suppressed by restricted light availability due to a combination of lower insolation levels incident at the surface ocean together with the presence of a relatively deep mixed layer. During winter, previously depleted surface nutrients are replenished through the entrainment of nutrient-rich deeper waters. This cycle is approximated by allowing deepening of the surface ocean mixed layer during the 'winter' season in SUE (as defined by mean monthly insolation being less than a prescribed threshold) with biological export effectively prohibited. If the water column becomes convectively unstable during this period, convective adjustments are made by pair-wise homogenization of cells down through the water column [*Wright and Stocker*, 1992]. To prevent excessive ventilation of the deep ocean occurring via this route, mixing depth is restricted according to the maximum observed mean mixed-layer depth (4.2.2).

'Deep water' formation

Realistic deep ocean T, S, and dissolved O_2 distributions are reproduced by transporting surface properties to depth via a conceptual sinking plume. Each 'winter' season, a water mass equal to that of the surface cell is allowed to sink until it reaches a cell with higher potential density (or the ocean bottom, whichever occurs first). T, S, and [O_2] properties are incorporated into the intervening cells in proportion to the mass of each call as a fraction of the total mass contained within the vertical interval over which the plume sinks. In order to further improve deep-water properties, the temperature of the sinking plume is reduced 4°C below mean annual SST (4.2.2) down to a minimum of -1°C.

Enhanced Southern Ocean mixing

Although between them the seasonal mixed-layer deepening and plume-generation go some way towards reproducing observed pelagic and benthic tracer fields, distributions at mesopelagic depths in the Southern Ocean, particularly of nutrients, are extremely poor. Lack of explicit vertical mixing in the ocean interior in this region due to convective and other sub-grid scale processes is counteracted by prescribing a mass exchange flux between layers lying at or below the maximum mixed-layer depth. This mixing is equivalent to a volumetric exchange of 50 Sv at 62.5°S and 10 Sv at 51.25°S.

4.2.3.2 Eddy diffusivity

The strength of vertical eddy diffusivity is varied down through the water column following *Weaver and Sarachik* [1991]. Use of a value for horizontal eddy diffusivity consistent with OGCMs and observational estimates of 1×10^3 m^2 s^{-1} [*Wright and Stocker*, 1992] is found to result in overly-steep meridional gradients in T, [PO_4], [H_4SiO_4], and [O_2] tending to develop in the Pacific and Indian Ocean basins. In order to improve these tracer fields a coefficient of 1×10^4 m^2 s^{-1} is adopted, comparable to values used in some ZOGCM [*Hovine and Fichefet*, 1994] and box models [*Archer et al.*, in press; *Rich et al.*, 1999]. This higher value can be justified on the basis that the effective diffusivity at a zonal scale is unlikely to be comparable to local rates [*Marchal et al.*, 1998b] and will need to account for the large-scale meridional mixing processes not represented, such as through gyre circulation [*Stocker et al.*, 1994].

4.2.4 The addition of deep-sea sediments

The Bern 2D model assumes a uniform ocean depth of 4000 m. However, in order to correctly represent the interaction between the ocean and deep-sea sediments a more realistic bathymetry must be prescribed [*Keir*, 1995]. As an initial step a mean global bathymetric profile (made on the basis of *ETOPO5* [1988] topography) is applied to each of the 16 grid points, imposing a maximum depth of 6000 m. Alteration of bathymetry in this way results in a slight reduction in total global ocean volume compared to the original model. In order to avoid biassing the residence time of water in each cell, global ocean volume is corrected by increasing the width of each ocean basin by ~9% and altering the depth of the base of each ocean layer. The lower boundary depths of the 8 vertical levels are now 47, 95, 144, 496, 1013, 2652, 3986, and 6000 m.

The depth resolution of the sediment modules employed to span the entire 6000 m depth of the ocean is chosen to maximize overall computational efficiency. Sensitivity analyses suggest that a depth interval of up to 500 m can be used with little distortion in the overall response of the global carbon cycle system to applied perturbations. However, since ocean layer thicknesses decrease and sedimenting fluxes increase as the ocean surface is approached, this resolution is progressively increased above 500 m depth in the ocean, to a minimum interval of 50 m.

4.3 Biogeochemical configuration

Final configuration of the global carbon cycle in SUE1608 requires the prescription of certain geochemical boundary conditions. In addition, there exist several unconstrained parameters associated with various biogeochemical processes that require a degree of optimization, with values chosen on the basis of achieving balanced model simulation 'success', as measured against a basket of present-day observational data. Such considered constraints include oceanic fields of [PO_4], [H_4SiO_4], and [Fe], particulate fluxes of POC, $CaCO_3$, and opal (and in particular the $CaCO_3$:POC rain ratio), and core-top $CaCO_3$ and opal sediment contents.

4.3.1 Geochemical boundary conditions

Since there is no explicit representation in SUE of processes lying outside of the atmosphere-ocean-sediment system (such

as terrestrial weathering) a number of geochemical boundary conditions need to be evaluated. Suitable values can be estimated on the basis of present-day observations, paleoclimate reconstructions, model simulations, or chosen simply to achieve a required system steady-state on an appropriate time scale.

4.3.1.1 Dissolved chemical input to the ocean

Coastal and continental shelf environments provide an important interface between terrestrial processes and the open ocean. In the absence of any explicit representation of these in SUE, dissolved chemical input to the ocean is simply applied directly to the surface ocean grid points in proportion to their relative surface area. Dissolved chemical inputs to SUE1608 are;

- Carbon and alkalinity (from Ca^{2+}) following *Walker and Opdyke* [1995]; some 20 and 40 Tmol a^{-1} for DIC and ALK, respectively.
- The ^{13}C isotopic signature of DIC is chosen in order to bring the system to a steady state characterized by an estimated pre-industrial mean oceanic $\delta^{13}C^{DIC}$ of -0.4‰ [*Yamanaka and Tajika*, 1996] over the long-term (>100 ka). A value for $\delta^{13}C^{DIC}$ of around -3.1‰ will achieve this.
- Global input of silicic acid arising from a combination of riverine influx, hydrothermal sources, and sea floor weathering (excluding the dissolution of biogenic opal) is taken to be 5.5 Tmol Si a^{-1} following *Tréguer et al.* [1995]. There is little difference between the delivery of aeolian-derived dissolved Si (assumed to be some 0.5 Tmol Si a^{-1} [*Tréguer et al.*, 1995]) in proportion to dust deposition fluxes or simply in proportion to surface ocean area. All (externally-derived) dissolved Si added to the ocean, a total of 6.0 Tmol Si a^{-1} therefore follows the other dissolved inputs in being delivered in proportion to surface area.

4.3.1.2 The delivery of aeolian material to the ocean

Supply of iron to the world ocean is thought to be dominated by riverine input [*Duce and Tindale*, 1991]. However, most of this iron is likely to be removed from the water column and sedimented in the neritic environment through a combination of low Fe utilization efficiency by coastal phytoplankton [*Sunda and Huntsman*, 1995] and high coastal productivity (with proportionally rapid scavenging). Indeed, the length scale of Fe penetration into the open ocean from coastal shelf areas has been estimated to be only ~16 km [*Johnson et al.*, 1997]. Iron input to the (open) ocean in the model is therefore assumed to be derived exclusively from aeolian dust deposited to the ocean surface.

Dust deposition rates are taken from the coupled GCM tracer advection and terrestrial ecosystem model simulations of *Mahowald et al.* [1999]. Fluxes to each grid point are derived from gridded GCM depositional fields in a similar manner to that used for deriving the physical surface forcings (4.2.2). However, on the basis that Fe originating from elevated near-shore dust deposition will suffer a similar fate to that of riverine Fe, coastal areas are masked out [*Fung et al.*, 2000]. Mean dust deposition fluxes ($f^{dust}_{(lat,lon)}$) to each grid point region in the model are thus given by

$$f^{dust} = \frac{\sum_{lat}\sum_{lon} H\left(D_{(lat,lon)} - 250\right) \cdot A_{(lat,lon)} \cdot f^{dust}_{(lat,lon)}}{\sum_{lat}\sum_{lon} H\left(D_{(lat,lon)} - 250\right) \cdot A_{(lat,lon)}} \qquad (4\text{-}3)$$

where the Heavyside function H excludes shelf areas defined by ocean depth <250 m.

Dust deposition tends to be a highly episodic process with a substantial proportion of the annual total being delivered in only a few individual events [*Jickells and Spokes*, in press; *Rea*, 1990, 1994]. However, the simple biological export scheme used in SUE is unlikely to gain much benefit from increased realism in this respect. Mean annual dust fluxes are therefore used.

Detrital input to deep-sea sediments derived only from the overlying surface aeolian flux can cause $CaCO_3$ and opal preservation to be underestimated in regions of very low dust supply (particularly the Southern Ocean and much of the Pacific). Additional material derived from continental shelves and slopes and reworked by bottom currents [*Bareille et al.*, 1994; *Seidov and Haupt*, 1999] may therefore play a significant role in such regions. To qualitatively account for these sources, neither of which are explicitly represented in SUE, detrital fluxes to deep-sea sediments are enhanced by 1.8 g m^{-2} a^{-1} [*Archer et al.*, 1998].

4.3.1.3 Neritic sediment accumulation

Calcium carbonate in coral reefs has been estimated to have been accumulating at 7-10 Tmol C a^{-1} over the last few thousand years [*Milliman*, 1993; *Munhoven and Francois*, 1996]. $CaCO_3$ is also deposited in non-reefal sediments within the neritic environment at a similar rate (~7.5 Tmol C a^{-1} [*Milliman*, 1993]). During glacial periods, low sea level stands resulted in extensive exposure of continental shelves. Intuitively, it would therefore seem highly likely that total global $CaCO_3$ accumulation rates were lower during the LGM than at present [*Berger*, 1982a; *Kleypas*, 1997; *Mundhoven and Francois*, 1994, 1996; *Walker and Opdyke*, 1995]. This presents a problem in constructing a modern simulation, since $CaCO_3$ in benthic sediments, with an adjustment time upwards of ~9 ka [*Archer et al.*, 1998] are likely to be far from steady state following the recent deglacial transition centred around 12 ka BP. This is supported by the observations of anomalous ^{14}C profiles in Pacific sediments [*Berelson et al.*, 1997; *Broecker et al.*, 1999b; *Keir and Michel*, 1993; *Oxburgh*, 1998; *Stephens and Kadko*, 1997]. For the purpose of generating a baseline simulation for parameter optimization, the carbonate system is assumed to be at steady state with respect to two thirds of the total estimated increase in $CaCO_3$ accumulation rate since the LGM, a net neritic sink of ~10 Tmol C a^{-1}. This is justified on the basis that following the rapid deglacial rise, sea level has been relatively stable for a period roughly equivalent to the *e*-folding time of the carbonate system.

An analogous situation might be expected to arise with respect to opal accumulation. That the global Si budget does not appear to balance at present, with an excess of loss

through deposition over dissolved inputs [*Tréguer et al.*, 1995] supports this hypothesis. However, since processes controlling neritic opal accumulation are much more poorly understood than for $CaCO_3$ no significant increase in opal accumulation rate since the LGM is taken into account in the construction of the baseline scenario.

4.3.2 Biological productivity

With a time step for biological uptake set at 1 day, unconstrained parameter values for export production are adjusted both in isolation and in concert in the search for an 'optimal' solution. The rate of net PO_4 uptake by (nutrient replete) siliceous phytoplankton ($u_{0,SP}^{PO_4}$) is set sufficiently high so as to enable realistic seasonal nutrient draw-down in the Southern Ocean. The value for net PO_4 uptake by (nutrient-replete) non-siliceous phytoplankton ($u_{0,NSP}^{PO_4}$) is then chosen in conjunction with the $CaCO_3$:POC export rain ratio ($r_{NSP}^{CaCO_3:POC}$) both to obtain a reasonable global rain ratio field and to balance the ocean DIC and ALK budgets over the long-term. Organic matter production is assumed to be entirely in particulate form with no DOM formation. The opal:POC export ratio from siliceous phytoplankton under iron replete conditions ($r_{0,SP}^{opal:POC}$) is chosen in order to obtain an oceanic inventory of dissolved Si consistent with *Tréguer et al.* [1995] and to produce a reasonable seasonal cycle in [H_4SiO_4]. Final optimized parameter values are summarized in Table 4-1. A degree of differential recycling is expected between opal and POC [*Dugdale and Wilkerson*, 1998] such that Si:C uptake ratios might be expected to be significantly different from the ultimate export ratio. However, the magnitude of this differential is highly dependent on assumptions made regarding grazing pressure, and can approach unity under conditions of low grazing intensity [*Dugdale et al.*, 1995]. The value for $r_{0,SP}^{opal:POC}$ is therefore reasonably consistent with Si:C uptake ratios reported under Fe-enriched conditions in the Southern Ocean [*Watson et al.*, 2000] and from incubation studies [*Hutchins and Bruland*, 1998] (Table 2-2).

Table 4-1 Parameter Values Resulting from Model Optimization

Parameter	Value
$u_{0,SP}^{PO_4}$	5.00 μmol kg^{-1} a^{-1}
$u_{0,NSP}^{PO_4}$	0.25 μmol kg^{-1} a^{-1}
$r_{0,SP}^{opal:POC}$	0.175
$r_{NSP}^{CaCO_3:POC}$	0.300
λ_{SP}	1.0
λ_{NSP}	1.0
$kscav_{dust}^{Fe}$	0.0750 a^{-1} (mol C m^{-2} a^{-1})$^{-1}$
$kscav_{POC}^{Fe}$	0.0025 a^{-1} (mol C m^{-2} a^{-1})$^{-1}$

4.3.3 Fe biogeochemical cycling

Initial constraints can be imposed upon basic aeolian Fe solubility in the surface ocean ($Fesol^{dust}$) through consideration of global dust input and estimated oceanic Fe residence times [*Jickells and Spokes*, in press]. Values for 'self-scavenging' and biogenic particulate scavenging rates ($kscav_{dust}^{Fe}$ and $kscav_{x}^{Fe}$, respectively) are adjusted in order to obtain a reasonable [Fe] field and produce surface ocean macro-nutrient concentrations (i.e., PO_4 and H_4SiO_4) approximately in line with observations. In the absence of any quantitative information regarding differential scavenging characteristics of the various materials comprising biogenic particulate matter, it is assumed that Fe is scavenged by POM, calcite, aragonite, and opal, in a 10:1:1:1 ratio (by molar flux density). Optimized values for Fe scavenging rate constants are summarized in Table 4-1. Aeolian Fe solubilities range from 1% in regions proximal to dust source areas such as low and mid latitudes in the Atlantic and Indian Oceans, to 3% in remote high southern latitudes and much of the Pacific Ocean, giving a mean global solubility of 1.17%. The influence of 'self-scavenging' reduces effective solubilities by up to ~70% under the highest dust deposition fluxes and surface dissolved Fe concentrations. The effective global mean solubility is therefore reduced to 0.69%, slightly lower than the range 0.8-2.1% estimated by *Jickells and Spokes* [in press].

4.3.4 "Nutrient trapping"

A common problem afflicting carbon cycle models is that of 'nutrient trapping' [*Najjar et al.*, 1992] – a positive feedback mechanism whereby nutrients released through the remineralization of particulate matter beneath highly productive up-welling regions are rapidly advected back to the surface, fuelling further productivity. This can lead to excessive nutrient concentrations and near-anoxic conditions at mesopelagic depths in such affected regions [*Maier-Reimer*, 1993; *Marchal et al.*, 1998b; *Najjar et al.*, 1992; *Yamanaka and Tajika*, 1996]. Distorted rain rates can also result in insufficient $CaCO_3$ preservation in the underlying sediments [*Heinze and Crowley*, 1997; *Heinze et al.*, 1999].

A number of different solutions to this highly undesirable feature have been proposed. The most common of these being to partition a substantial fraction of new production into the form of dissolved organic matter (DOM), allowing nutrients to advectively 'leak' out of the up-welling system. This fraction can be either explicitly prescribed [*Marchal et al.*, 1998b; *Najjar et al.*, 1992; *Paillard et al.*, 1993; *Sarmiento et al.*, 1988; *Yamanaka and Tajika*, 1997] or derived internally as a result of grazing and cell lysis within a multi-trophic mechanistic biological scheme [*Six and Maier-Reimer*, 1996]. However, the DOM export fraction required in order to largely alleviate this problem is substantial, typically being more than 50% (Table 4-2).

Although biogeochemical 'fixes' have tended to be chosen in order to remove nutrient trapping from equatorial up-welling systems, it has been suspected that it is the representation of ocean circulation that is at fault [*Yamanka*

and Tajika, 1996]. *Aumont et al.* [1999] found that increasing meridional resolution in the Pacific can vastly improve the simulation of nutrient transport by the equatorial undercurrent (EUC) into the region of equatorial divergence and up-welling and result in very little nutrient trapping. Application of a numerical scheme with relatively low diapycnal diffusivity has also been found to lessen nutrient trapping in the equatorial Atlantic [*Oschlies and Garcon*, 1999]. There must be serious concerns regarding attempts made to correct for local problems in the representation of the physical ocean through what is effectively the distortion of global biogeochemical cycling. In any case, there is scant observational evidence to support the magnitude of the required DOM fraction, with some model results suggesting that DOC is unlikely to constitute more than 10% of the total organic carbon transport out of the equatorial Pacific [*Aumont et al.*, 1999].

Nutrient trapping is muted in the Equatorial Pacific because the EUC (the primary source of up-welled nutrients) is tightly confined in the vertical so that the proportion of settling POM remineralized within it is low. Instead, nutrients are predominantly released at depths below the EUC and are thus prevented from feeding directly back into the equatorial divergence and up-welling. On this basis, an oceanographic topological 'fix' is employed in SUE1608. In this, the depth at which remineralization begins is artificially deepened; 400 m in the equatorial Atlantic and Pacific with 200 m in the equatorial Indian Ocean.

4.4 The 'present-day' in SUE1608

A modern (pre-industrial) baseline simulation is generated by running SUE1608 for 500 ka following an initial 50 ka spin-up, sufficient to bring even the slowest adjusting part of the system approximately into equilibrium (ocean ^{13}C with an *e*-folding time of order 100 ka). Final model state is characterized by an atmospheric CO_2 concentration of 269 ppmv, slightly lower than pre-industrial estimates of 278 ppmv [*IPCC*, 1990], with a ^{13}C isotopic signature of -6.2‰, some ~0.3‰ too high [*Smith et al.*, 1999]. The reasons for the discrepancies in atmospheric composition probably lie mainly in a combination of the simplistic partitioning of biological export between just two phytoplankton groups, the representation of convective regimes at high latitudes, and lack of true seasonality. Since the primary focus of this study is on the dynamical behaviour of the system over an extended time period there is little to be gained from over-tuning model steady-state. Indeed, it would be detrimental to the ability of SUE1608 to produce a realistic glacial-interglacial response if deficiencies in physical ocean representation were to be entirely compensated for through the alteration of biogeochemical processes. Mean ocean DIC, ALK, PO_4, and H_4SiO_4 concentrations of 2234, 2370, 2.1, and 74.5 μmol kg^{-1}, respectively, are all in line with pre-industrial estimates [*Tréguer et al.*, 1995; *Yamanka and Tajika*, 1996], as is a mean ocean $\delta^{13}C^{DIC}$ of 0.37‰ [*Yamanka and Tajika*, 1996]. Total POC export out of the euphotic zone is 8.8 GtC a^{-1}, similar to current model estimates of 7.5-10.0 GtC a^{-1} as summarized in Table 4-2. $CaCO_3$ export is 1.3 GtC a^{-1}, giving a mean ocean $CaCO_3$:POC export rain ratio of 0.14, again consistent with estimates lying in the range 0.08-0.25. Global opal export is 137 Tmol a^{-1}, somewhat lower than previous model-derived estimates of 170-275 Tmol a^{-1} but close to the value of ~120 Tmol a^{-1} obtained by *Tréguer et al.* [1995] from mass balance considerations. Model parameter values are summarized in Appendix IV.

The degree of 'success' of this simulation in reproducing the characteristics of the modern state of the global ocean carbon cycle is now evaluated in more detail against a variety of ocean tracer, biogenic flux, and sediment compositional fields.

Table 4-2 Global New Production Estimates from Global Carbon Cycle Models

Model class	Fnp^{POC} (GtC a^{-1})	Fnp^{DOC} (GtC a^{-1})	Fnp^{TOC} (GtC a^{-1})	$r^{DOC:TOC}$	Fnp^{CaCO_3} (GtC a^{-1})	$r^{CaCO_3:POC}$	Fnp^{opal} (Tmol a^{-1})	Reference
3D OGCM	10	0	10	0.00	0.80	0.08	n/a	*Yamanaka and Tajika* [1996]
3D OGCM	8	3	11	0.27	-	-	n/a	*Yamanaka and Tajika* [1997]
3D OGCM	9.4	1.7	11.1	0.15	-	-	n/a	*Six and Maier-Reimer* [1996]
3D OGCM	8.9	0.0	8.9	0.00	1.80	0.20	170	*Heinze et al.* [1999]
3D OGCM	-	-	-	0.12	-	-	n/a	*Aumont et al.* [1999]
3D OGCM	7.5	0.0	7.5	0.00	1.65	0.22	n/a	*Archer et al.* [1998]
3D OGCM	-	-	12-15	0.80	-	-	n/a	*Najjar et al.* [1992]
3D OGCM	11.0	0.0	11.0	0.00	2.18	0.20	275	*Archer et al.* [2000]
ZOGCM	-	-	6.3-10.8	0.50	0.38-0.65	0.06	n/a	*Marchal et al.* [1998b]
Box	8.5	0.0	8.5	0.00	-	-	n/a	*Rich et al.* [1999]
(SUE)	8.8	0.0	8.8	0.00	1.3	0.14	137	This study

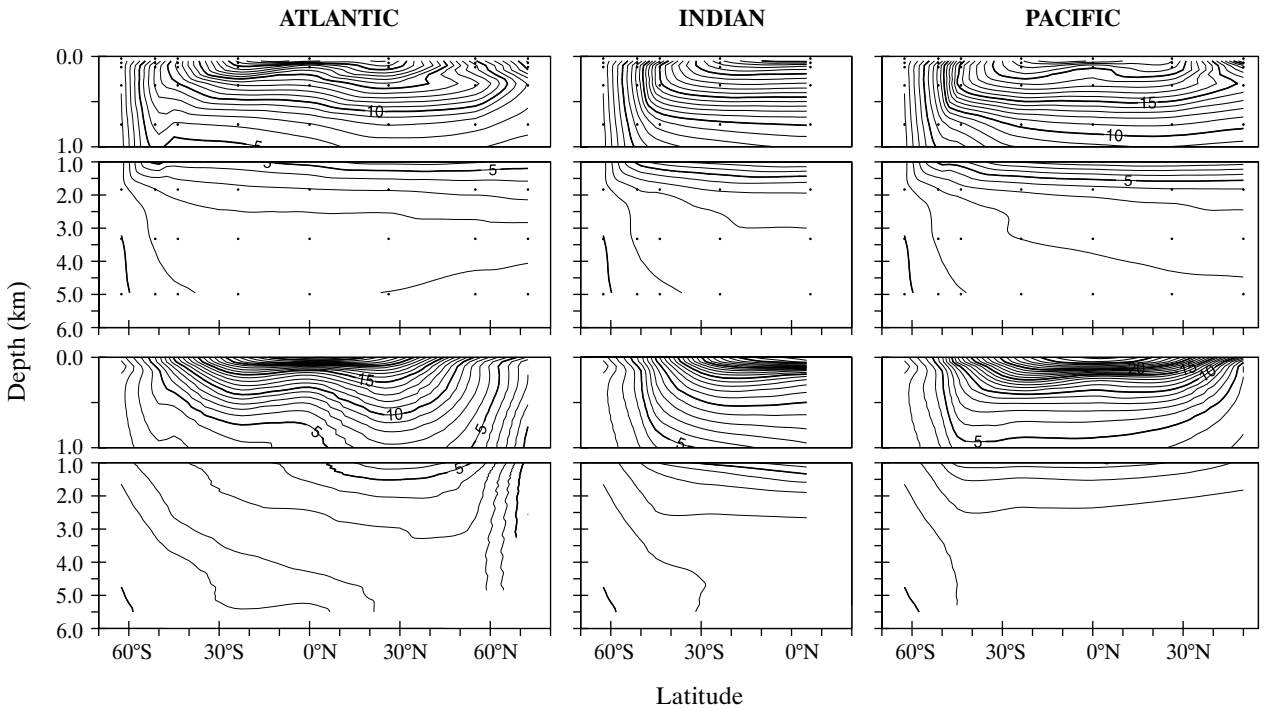

Figure 4-4 Ocean temperature field (°C); model results (top) compared with observations [*Levitus et al.*, 1994c] (bottom).

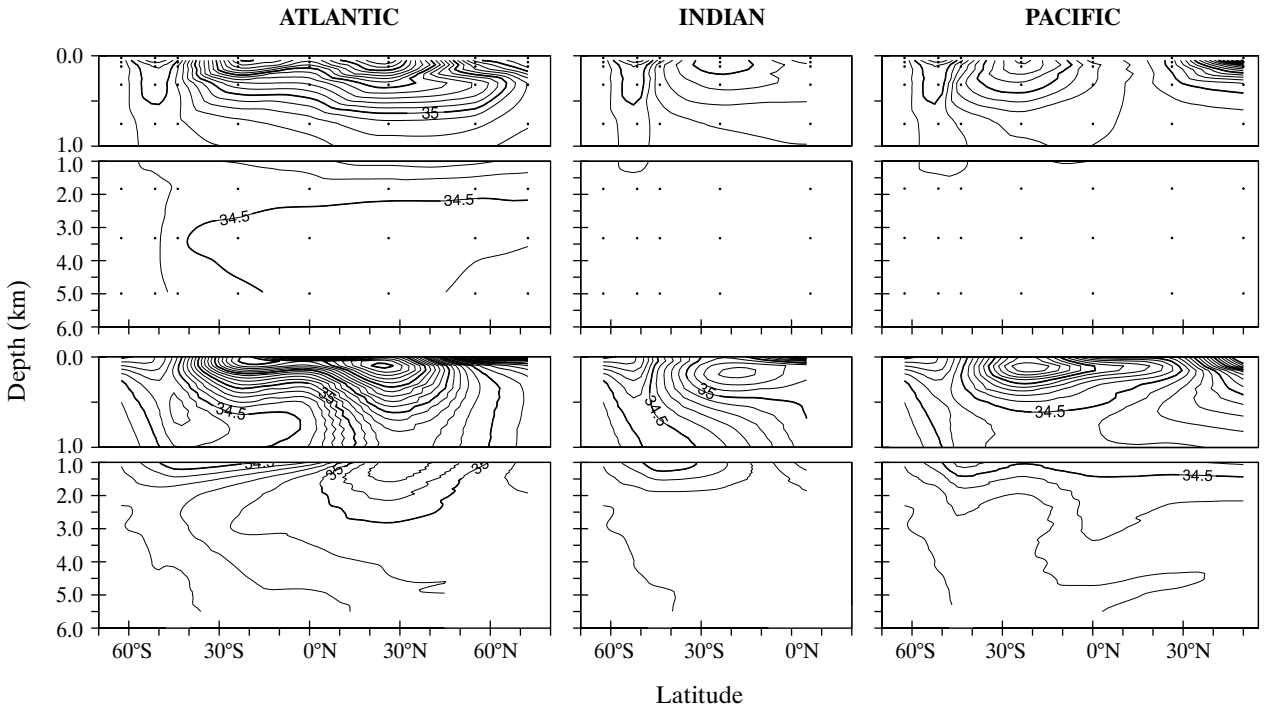

Figure 4-5 Ocean salinity field (‰); model results (top) compared with observations [*Levitus et al.*, 1994b] (bottom).

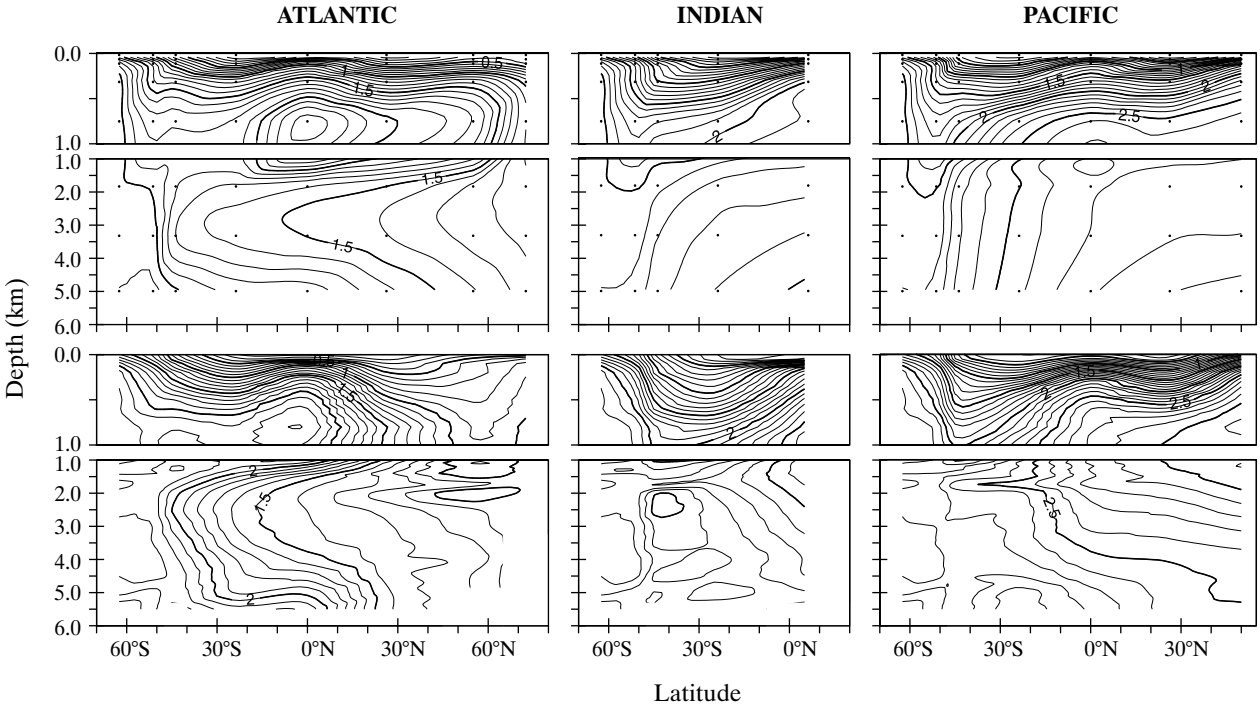

Figure 4-6 Ocean PO_4 field (μmol kg^{-1}); model results (top) compared with observations [*Conkright et al.*, 1994] (bottom).

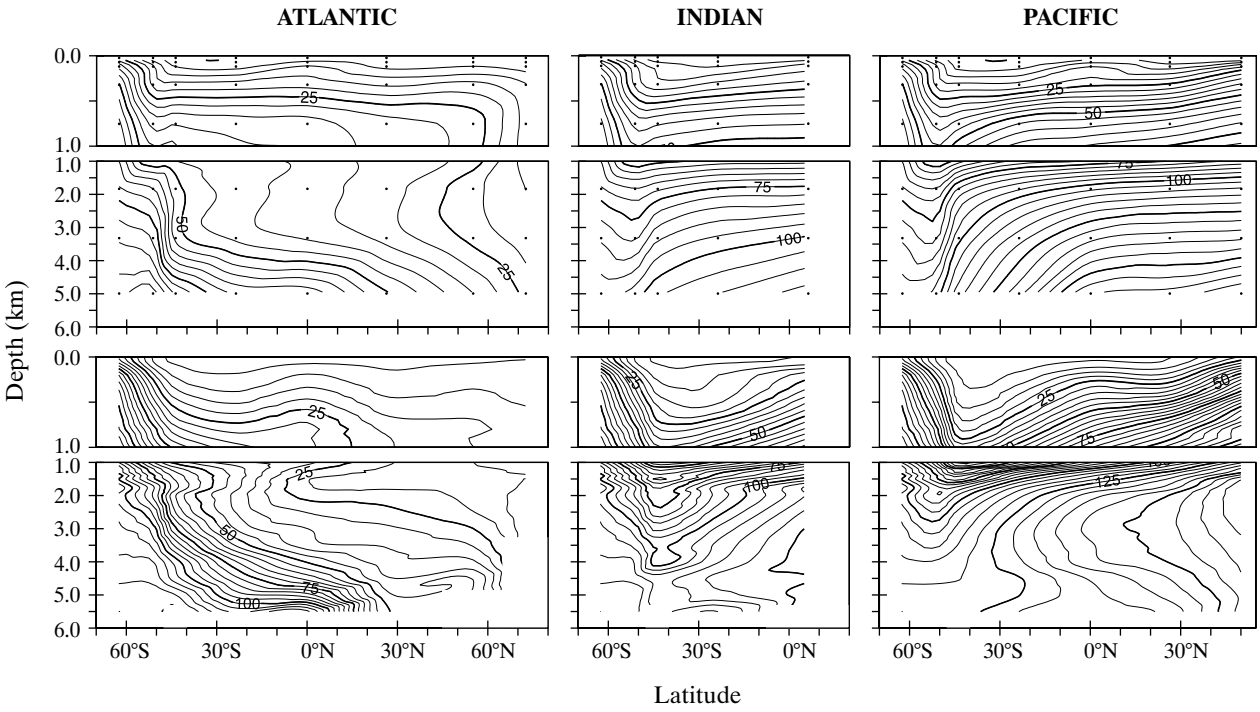

Figure 4-7 Ocean H_4SiO_4 field (μmol kg^{-1}); model results (top) compared with observations [*Conkright et al.*, 1994] (bottom).

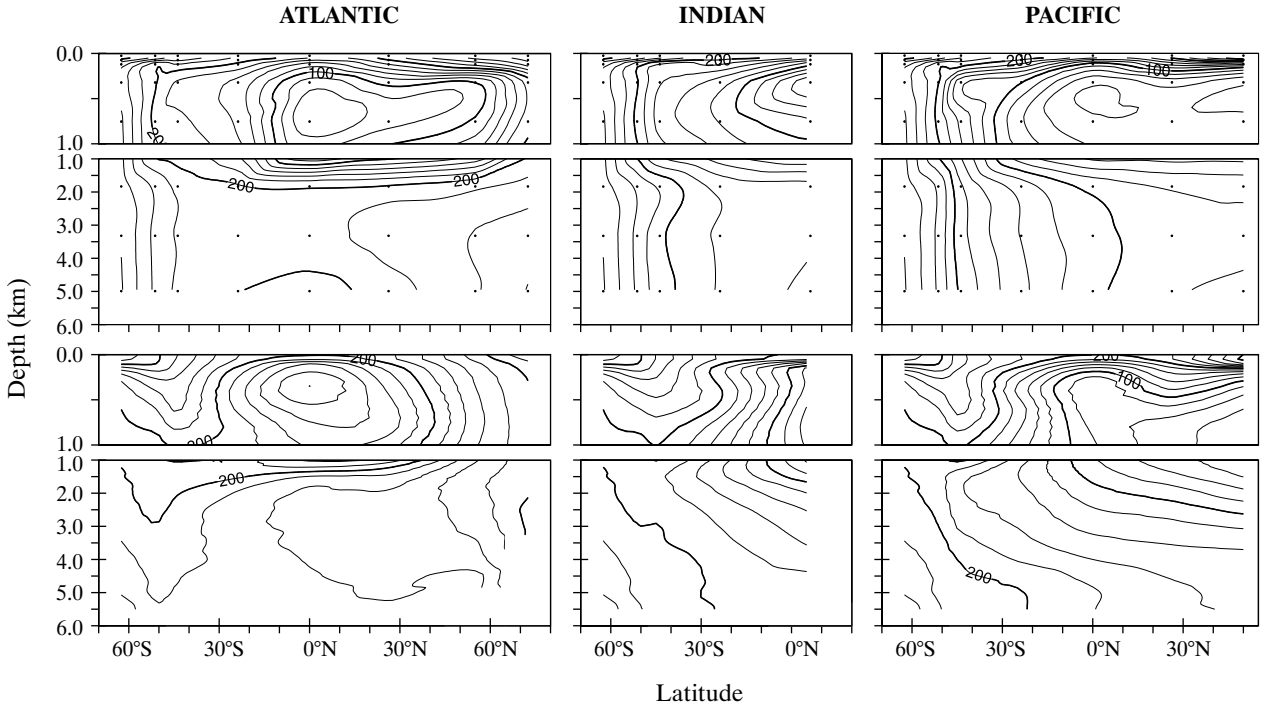

Figure 4-8 Ocean dissolved O_2 field (μmol kg^{-1}); model results (top) compared with observations [*Levitus et al.*, 1994a] (bottom).

4.4.1 Ocean tracer fields

4.4.1.1 Temperature and salinity

The annual mean temperature field in the model (Figure 4-4) is generally quite realistic. However, there are several obvious deficiencies; the thermocline in all three ocean basins is too weak and high latitude temperature distributions tend to be poorly reproduced, particularly in the north Atlantic (associated with the formation of North Atlantic Deep Water (NADW)) and in the north Pacific where there appears to be inadequate up-welling and/or wintertime convective overturning. The weak thermocline structure may exacerbate nutrient trapping problems in the model, as a temperature overestimate of ~5°C (typical of much of the mesopelagic zone) will result in an overestimate in the dissolution rate of settling opal of ~50% (assuming a Q_{10} of 2.3).

Salinity fields (Figure 4-5) are much more poorly reproduced than those for temperature, with obvious problems associated with the formation and transport of NADW and Antarctic Intermediate Waters. Fortunately, with prescribed ocean circulation, salinity plays little part in controlling the global carbon cycle. Even where aqueous carbonate chemistry is moderately sensitive to salinity such as its influence on CO_2 fugacity in the surface ocean, salinity values are restored to and thus always follow observations.

4.4.1.2 Phosphate

The ocean phosphate field is generally fairly well reproduced by the model (Figure 4-6) particularly in the upper water column (< 1000 m), although there is still some distortion of equatorial Pacific profiles associated with residual nutrient trapping. As with temperature, circulation-related problems occur at high latitudes although to a lesser degree, since remineralization processes within the water column dominate over advection in controlling vertical PO_4 distributions. Contrary to observations there are no distinct mid-depth nutrient maxima in either the northern Indian or Pacific basins, suggesting potential deficiencies with the scheme used for POM remineralization. Lack of any explicit representation of the diagenetic alteration of particulate organic matter in deep-sea sediments may also play a role.

4.4.1.3 Silicic acid

As with phosphate, the model is reasonably successful in reproducing general trends in the H_4SiO_4 field (Figure 4-7). However, again there is a failure to reproduce observed ocean interior nutrient maxima in both the Pacific and Indian basins. In addition, the degree of opal remineralization appears to be slightly too extensive in surface layers (above ~500 m), possibly associated with the weak thermocline structure as noted previously. The model also underestimates the gradient of the deep H_4SiO_4 nutricline centred on the 75 μmol kg^{-1} contour. That the

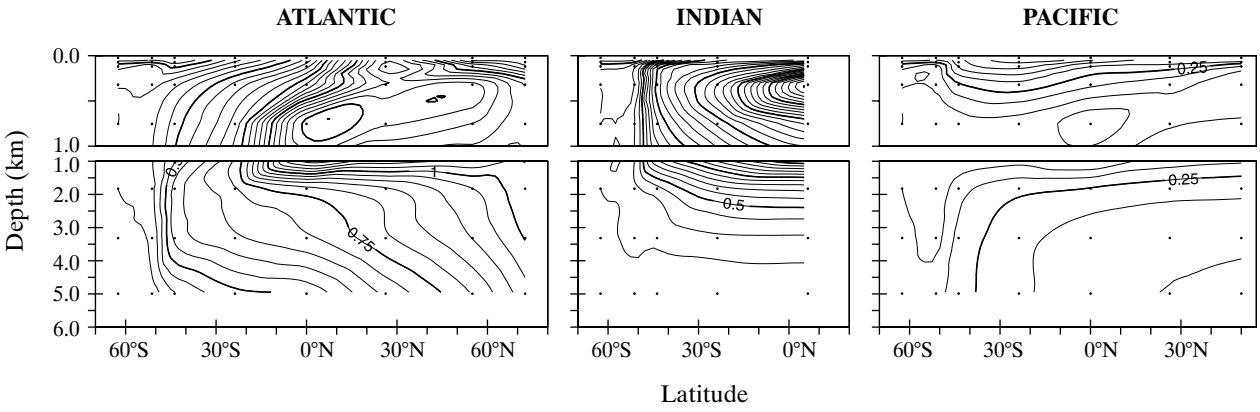

Figure 4-9 Ocean total dissolved Fe field (nmol kg^{-1}); model results only.

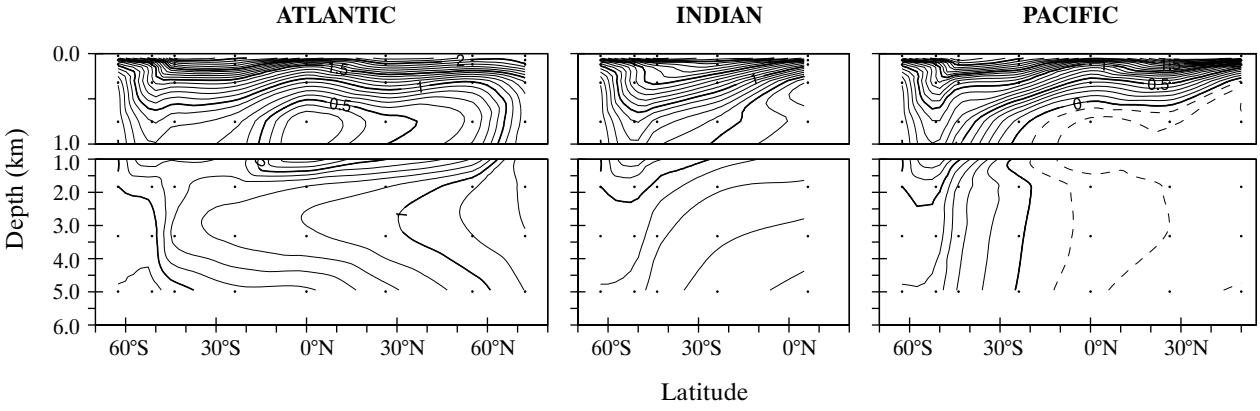

Figure 4-10 Ocean $\delta^{13}C_{DIC}$ field (‰); model results only.

remineralization of POM and opal are represented and controlled in very different ways within SUE supports the notion that it is ocean structure and/or circulation that is predominantly to blame for such failures.

4.4.1.4 Dissolved oxygen

The dissolved oxygen field (Figure 4-8) is arguably the least successfully reproduced. That this should be so is perhaps not entirely surprising considering that its distribution is highly dependent on seasonal high latitude processes to delivering O_2 to the ocean interior, processes that are poorly-represented in the model. Despite this, $[O_2]$ minima beneath the equatorial Atlantic and at intermediate depths in the northern Indian Ocean are simulated, although the northern Pacific minima is clearly too shallow and weak.

4.4.1.5 Total dissolved iron

Figure 4-9 shows the model field of total dissolved iron. Unlike other chemical ocean properties which have been routinely analysed for many years, measurements of [Fe] are a relatively recent innovation with the result that there is no comparable global data set available. The following comparisons can still be drawn between predicted and observed [Fe], although care must be taken since model values represent zonal and depth-averaged annual means while measurements are discrete in space and time;

- Fe concentrations appear to be over-estimated in the north Atlantic with the existence of a prominent mesopelagic maximum (>1.0 nmol kg^{-1}) whereas JGOFS data suggests a more steady increase down through the water column and not reaching a maximum (~0.7 nmol kg^{-1}) until a depth of 2000 - 3000 m [*Martin et al.*, 1993].
- Relatively high Fe concentrations observed in the northeast Pacific [*Martin and Gordon*, 1988; *Martin et al.*, 1989; *Johnson et al.*, 1997] are not captured by the model with deep-water concentrations being too low. The existence of a mesopelagic maximum is predicted, however.

- The model matches observations at depths shallower than ~500 m in the equatorial Pacific [*Coale et al.*, 1996; *Gordon et al.*, 1997], although deeper concentrations are again underestimated.
- In the Southern Ocean there is generally good agreement between model and observed Fe concentrations at shallow and intermediate depths (< 1500 m) in the Drake Passage [*Martin et al.*, 1990], the SE Pacific sector [*de Baar et al.*, 1999], and the Australian sector [*Sohrin et al.*, 2000]. However, once more, values in the deep ocean tend to be underestimated.

It is likely that SUE1608 fails to reproduce the enhanced Fe concentrations observed in the deep ocean due to the lack of any representation of the return to the ocean of dissolved Fe derived from material deposited to the sediments. This diagenetically-released Fe may be largely restricted to the deep ocean due to a constant downward scavenging pressure. If so, this omission may not significantly affect Fe supply to the surface ocean (a critical factor in controlling biological productivity).

4.4.1.6 $\delta^{13}C^{DIC}$

Figure 4-10 shows the field for the ^{13}C isotopic signature of total dissolved inorganic carbon ($\delta^{13}C^{DIC}$). In the Atlantic basin model $\delta^{13}C^{DIC}$ distributions are reasonably similar to observations (not shown) [*Yamanaka and Tajika*, 1996]. However, surface values are generally too high across all three basins (responsible for the over-prediction in atmospheric $\delta^{13}C$). The strength of mid-depth minima underlying the equatorial Atlantic and northern Pacific are also incorrectly predicted.

4.4.2 The biological pump

Meridional distributions of annual mean nutrient concentrations and biological fluxes are shown in Figure 4-11 for each of the three ocean basins. It can be seen that observed zonally averaged surface ocean PO_4 concentrations are reasonably reproduced, albeit slight too low. Observed trends in H_4SiO_4 concentrations with deplete conditions in much of the low- and mid-latitude world ocean but rising steeply south of the Antarctic Polar Front are also correctly predicted, although again there is a general slight under-prediction in concentrations. However, there is a complete failure to capture high [H_4SiO_4] values observed in the north Pacific, suggesting serious deficiencies in ocean circulation and/or biological representation in this region. The control that silicic acid availability exerts on the partitioning of POC between siliceous and non-siliceous phytoplankton in the biological model is exemplified by the export rain ratio of $CaCO_3$:POC. For instance, in the Southern Ocean where H_4SiO_4 is not limiting to siliceous phytoplankton, export by this class dominates the biological system and net $CaCO_3$:POC is extremely low.

The availability of iron exerts a number of different controls on export production. Excess PO_4 remaining in the equatorial Pacific up-welling zone is a result of the high degree of Fe limitation there, while a combination of summertime Fe limitation and wintertime deep mixing act to limit annual production in the Southern Ocean and north Pacific. High concentrations of Fe present in surface waters in the mid and northern latitude Atlantic and Indian Oceans are due to their relative proximity to dust source regions, with concentrations declining sharply towards the south as the remote Southern Ocean is approached. Low dust deposition rates to the low- and mid-latitude Pacific restricts Fe availability preventing the complete utilization of PO_4 advected from the equator and high latitudes. Iron also plays an important role in determining the efficiency with which H_4SiO_4 is utilized by siliceous phytoplankton per unit carbon fixed (2.2.3.3). For instance, while POC export derived from siliceous phytoplankton is slightly greater at the equator in the Atlantic compared to that in the Pacific, greater Atlantic Fe availability allows increased H_4SiO_4 utilization efficiency resulting in opal export being suppressed.

The meridional profile of (total) $\delta^{13}C^{POC}$ in each of the three basins is very similar, with a relatively constant degree of ^{13}C fractionation in exported POC between -19 and -21‰ over mid and low latitudes. South of around 30°S, however, the isotopic signature decreases sharply to a value of around -28‰ by 60°S, while a less steep decrease with latitude is apparent north of 30°N, reaching a minimum of only about -25‰. These model distributions are consistent with measurements made on suspended particulate organic matter recovered from along meridional transects (not shown) [*Bentaleb et al.*, 1998; *Goericke and Fry*, 1994; *Hofmann et al.*, 1999; *Popp et al.*, 1999], sharing remarkably similar features and values. Differences do arise in the location and slope of the transition zone lying either side of the low- and mid-latitude $\delta^{13}C^{POC}$ 'plateau'. This is probably simply an artifact of the low meridional resolution of SUE1608 rather than reflecting anything more fundamental regarding biological export or ^{13}C fractionation. However, observed data do exhibit a significant degree of scatter with extreme values lying up to ±5‰ from the general trend. While this may be partly due to the high degree of spatial averaging inherent in the model it may also reflect variability in ecosystem assemblage and the physiological state of individual cells [*Burkhardt et al.*, 1999; *Hinga et al.*, 1994], both of which are poorly accounted for in the biological scheme employed in SUE.

There is a reasonable similarity between model-generated settling fluxes of POC and $CaCO_3$ and observational data [*Tsunogai and Noriki*, 1991] (not shown). Water-column profiles of $CaCO_3$ are well reproduced with little dissolution occurring in the water column below 500-1000 m, although observations indicate a greater degree of POC remineralization at depth than predicted by the model. Inter-regional contrasts are generally correctly simulated, with lowest POC fluxes in the ocean associated with mid-latitude gyre regions. However, problems in the representation of the equatorial Pacific up-welling zone results in a significant overestimation of POC fluxes. As $CaCO_3$ fluxes here are of the correct magnitude, the $CaCO_3$:POC rain ratio is then distorted.

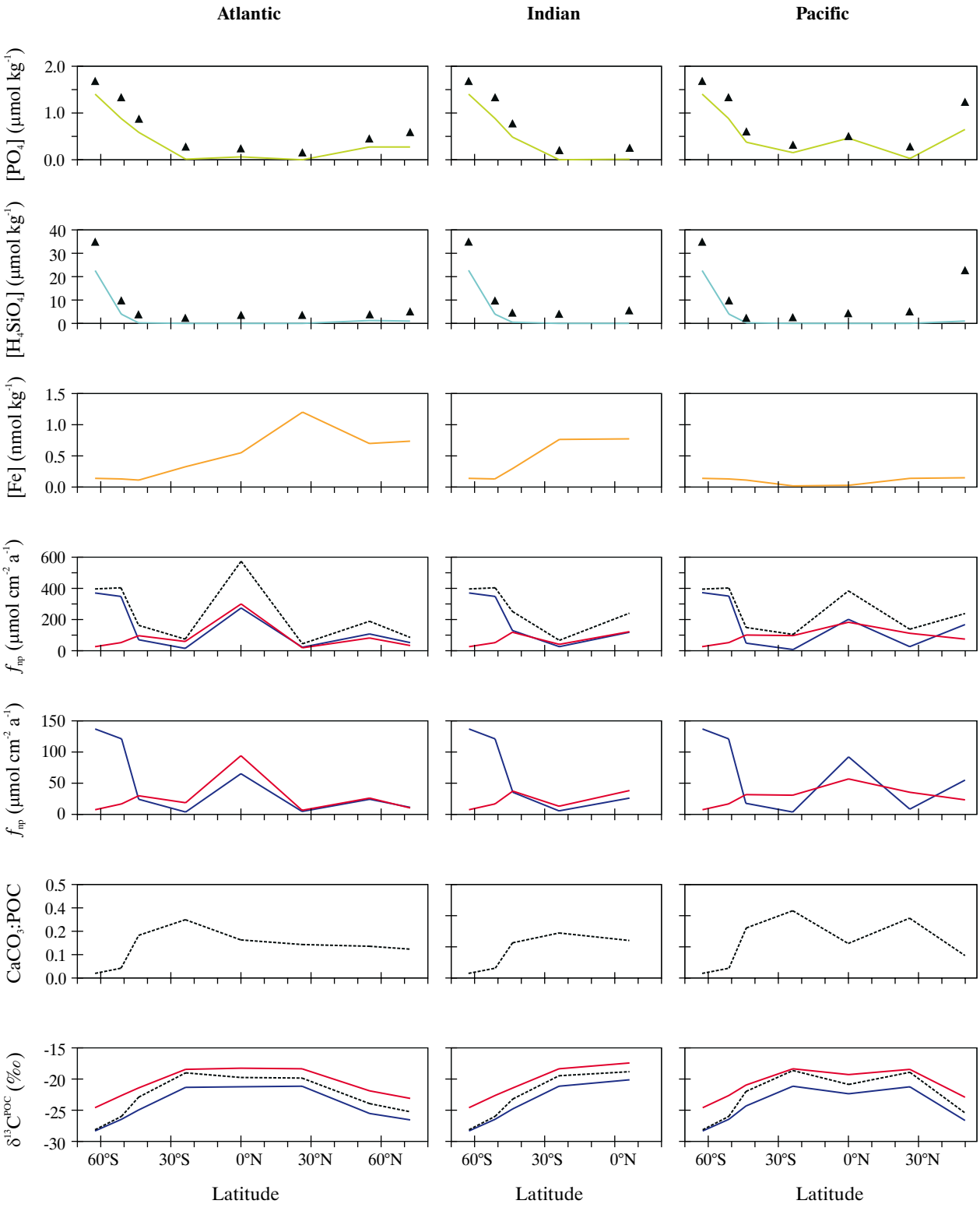

Figure 4-11 Meridional profiles of ocean surface characteristic in each ocean basin in SUE1608. Shown (from top to bottom) are; mean annual PO_4 concentrations (model values in green, observations (at 30 m depth) [*Conkright et al.*, 1994] marked as filled triangles); mean annual H_4SiO_4 concentrations (model values in light blue, observations (at 30 m depth) [*Conkright et al.*, 1994] marked as filled triangles); mean annual Fe concentrations (orange); POC export fluxes from siliceous phytoplankton (dark blue), non-siliceous phytoplankton (red), together with the total flux (black dotted); opal export (dark blue) and $CaCO_3$ export (red) fluxes; $CaCO_3$:POC rain ratio (black dotted); and $\delta^{13}C^{POC}$ of siliceous phytoplankton (dark blue), non-siliceous phytoplankton (red), together with the total flux (black dotted).

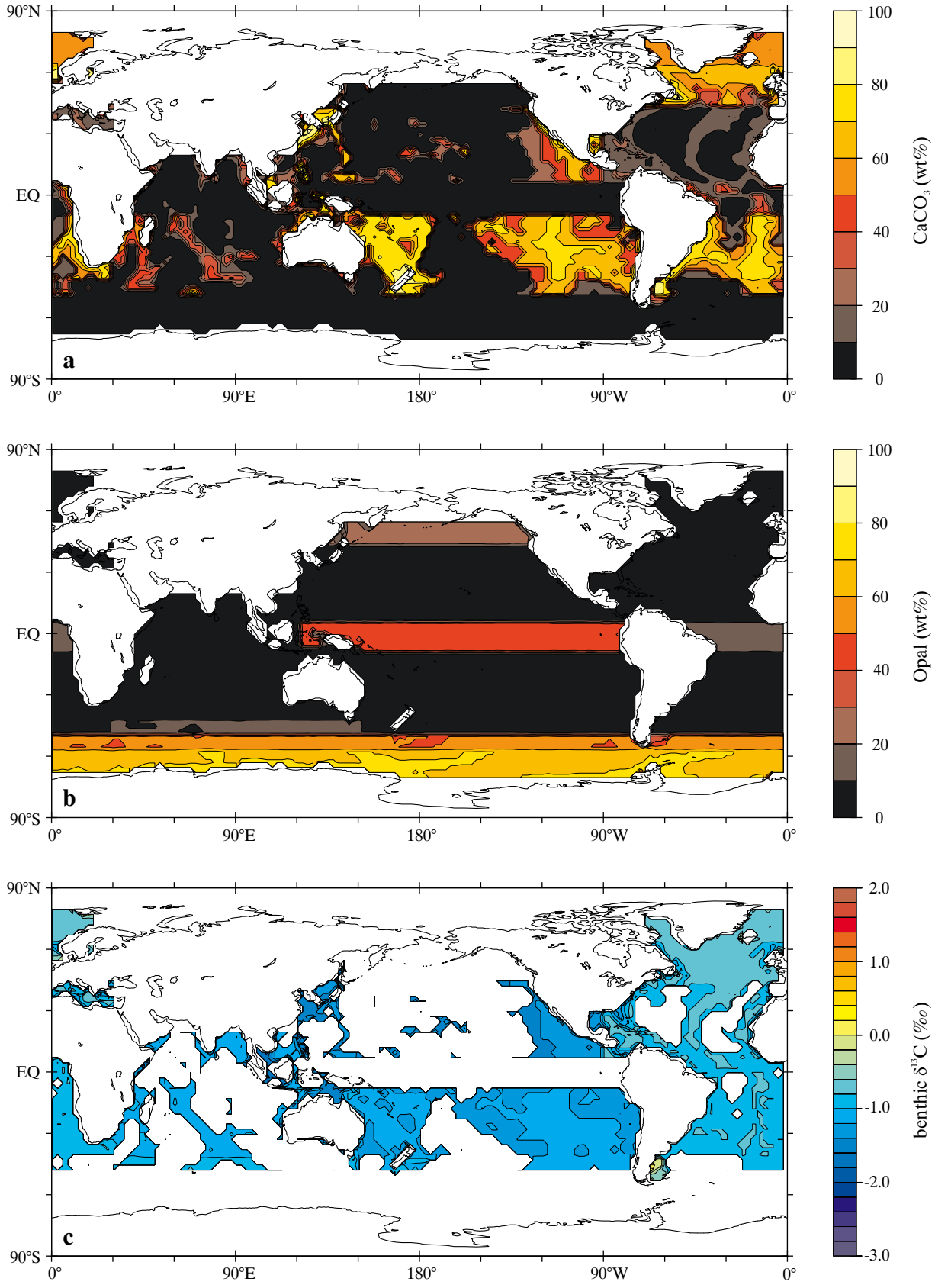

Figure 4-12 Modern steady-state distributions of surface sediment characteristics generated by SUE1608; wt% $CaCO_3$ (top), wt% opal (middle), and benthic foraminiferal $\delta^{13}C$ (bottom) assuming the *Globigerina bulloides* ^{13}C fractionation relationship (2-63). Spatial resolution is gridded at 2.5°×2.5°.

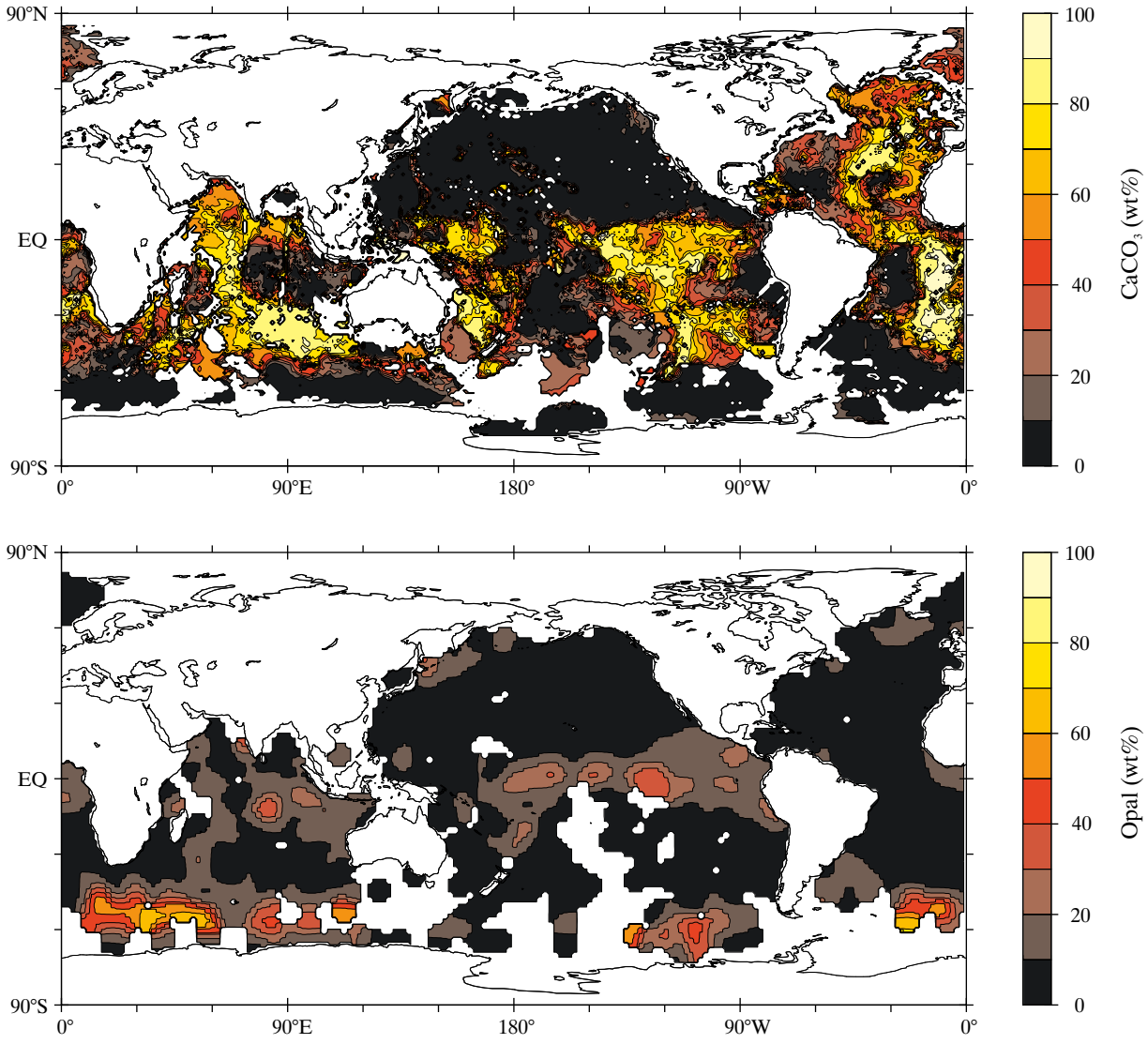

Figure 4-13 Observed core-top sediment composition distributions; wt% $CaCO_3$ (top) [*Archer*, 1996b], and wt% opal (middle) [*Archer*, pers com].

4.4.3 Sediment composition

The composition of deep-sea sediments is controlled by a combination of benthic environmental conditions (physical and chemical) and particulate matter rain rates (in turn affected by a combination of ocean properties throughout the water column and surface ocean biological productivity). Since surface sediment properties effectively reflect an integrated state of ocean biogeochemical cycling, their global distribution can be used as a powerful diagnostic of model operation. Figure 4-12 shows predicted distributions of surface sediment $CaCO_3$ (as calcite) and opal content, together with benthic foraminiferal $\delta^{13}C$. Equivalent observational data (where available) is shown in Figure 4-13.

It can be seen that there is a good correspondence between predicted $CaCO_3$ contents and observations for many regions of the world ocean. In particular, the apparent depth of the calcite lysocline appears to be extremely well reproduced in the south Atlantic and south Pacific. However, there are a number of notable problem areas. Firstly, there is too little $CaCO_3$ preservation in the equatorial Pacific. This is most likely a result of an under-predicted $CaCO_3$:POC rain ratio, since the poor representation of biogeochemical cycling in this region produces excessive POC export which in turns drives enhanced $CaCO_3$ dissolution in the underlying sediments. This problem is not specific to SUE1608 and is apparent in 3D OGCM carbon cycle models [*Heinze and Crowley*, 1997; *Heinze et al.*, 1999], although nutrient trapping tends to be much more localized in these. Similar arguments

apply to the equatorial Atlantic. The other major areas of concern are the Indian Ocean and northern mid latitude Atlantic where the zonally-averaged nature of ocean circulation tends to overly-restrict nutrient supply and thus potential $CaCO_3$ export. That these two regions are both characterized by high dust deposition fluxes suggests that the influence of Fe availability on H_4SiO_4 utilization efficiency (2.2.3.3) may potentially be overstated, distorting the POC partitioning between the two phytoplankton groups and with it the net $CaCO_3$:POC rain ratio. The aragonite lysocline is predicted to lie at a depth of around 2000-3000 m in the Atlantic and <1000 m in the Pacific, both consistent with observations [*Balsam*, 1983; *Berger*, 1977].

Global distributions of core-top opal content are also generally reasonable. However, little opal accumulation is predicted for the Indian Ocean contrary to observations, whereas opal contents in the equatorial Atlantic and north Pacific are slightly over-estimated. The only other area of significant mismatch concerns the Southern Ocean, where a maximum in opal content occurs in the southernmost grid point region (centred on 62.5°S) in contrast to observations of a relatively tightly constrained circumpolar 'belt' of maximum opal accumulation further to the north at around ~55°S. This is likely to be primarily an artifact of the low meridional resolution in this region employed in the model.

The distribution of the benthic foraminiferal calcite isotopic signature ($\delta^{13}C^{foram}$) in the model is also shown (Figure 4-12c). A trend is visible across the ocean with maximum values of -0.6 ‰ in the north Atlantic, through -1.1 ‰ in the sub-polar Antarctic, to less than -1.5 ‰ in parts of the northwestern Pacific. This oceanic trend is comparable to that reconstructed from the analysis of deep-sea sediment cores [*Matsumoto and Lynch-Stieglitz*, 1999; *Michel et al.*, 1995], although a few tenths of a per mill less in the total range spanned. It should be noted that due to vital differences between species used for observational analysis and those represented in the model, absolute values are not directly comparable.

4.5 An improved representation of the Southern Ocean and global Si cycling

One of the most noticeable deficiencies resulting from the ocean configuration adopted in SUE1608 was in the inability of the model to resolve the circumpolar opal maximum observed in the Southern Ocean. There is a danger that any significant failure in correctly representing what is the primary opal sink in the world ocean might distort the dynamics of the global silica cycle in the model and thereby degrade the applicability of SUE1608 to many of the mechanisms for glacial-interglacial CO_2 variability. In addition, use of a single grid point region covering the entire polar Southern Ocean makes any attempt in a realistic representation of variability in sea ice extent (thought to be a key mechanism driving CO_2 changes [*Stephens and Keeling*, 2000]) problematic. An alternative configuration is therefore introduced to allow more detailed analysis of the global silica cycle and of mechanisms for glacial-interglacial change located in the Southern Ocean.

The ocean configuration of the improved model is derived from Bern 2D ZOGCM [*Marchal et al*., 1998a; *Stocker and Wright*, 1996] as previously for SUE1608 (4.2.1). However, rather than amalgamating the two zonal regions in the parent model south of 55°S these are now kept discrete. Meridional resolution is further enhanced by sub-dividing these two 7.5° zones into sub-zones of width 2.5°. Ocean circulation in these regions is derived by assuming that each of the sub-zones is characterized by the same vertical velocity as its parent zone. Meridional velocities across the boundaries separating the sub-zones are obtained by linearly interpolating between velocities at 55°S and 62.5°S in the Bern 2D circulation, and extrapolating south of 62.5°S. A total of six zonal regions now replaces the single zone south of 55°S in SUE1608 – with a total of 21 grid points the new model is designated 'SUE2108'. The same parameter values as optimized for SUE1608 (4.3.2) are adopted, resulting in a similar baseline model state.

4.5.1 Sedimentary opal distributions

Figure 4-14a shows the global distribution of surface sediment opal content in SUE2108. It can be seen that a distinct circumpolar belt of maximum opal content is now resolved. The meridional location of this feature is centred on ~60°S with maximum opal contents reaching around 75 wt%, both reasonably consistent with observations [*Archer*, pers com; *Broecker and Peng*, 1982]. Preservation efficiencies in these high opal content sediments have been recently estimated at some 6.8% [*DeMaster*, 2000], comparable to model predictions of 7-9% (Figure 4-14c). There is an apparent southerly offset (~3-4°) in the latitude of maximum opal content relative to the location of peak surface ocean biogenic opal export rates (not shown). This is a result of the trend of increasing H_4SiO_4 concentrations at intermediate and shallow depths (< 4000 m) with southerly latitude (Figure 4-7), producing a similar trend in the preservation efficiency within the water column (Figure 4-14b) and displacing southwards peak opal fluxes reaching the sediment surface. Near to the Antarctic continental shelf, model sediment preservation efficiencies of 5-7% are also comparable to observational-based estimates in the Ross Sea of around 6% [*DeMaster*, 2000]. A consequence of the improved representation of the Southern Ocean silica cycle is a slight reduction in equatorial and north Pacific opal contents, bringing them more in line with observations. Primary observed variability in sedimentary opal distributions not captured by the model is now intra-zonal, beyond the ability of a zonally-averaged model to prognostically generate.

4.5.2 Re-evaluation of the opal diagenesis module

Previously, the opal diagenesis module was validated with the aid of a simple box model (3.2.3.5). Re-validation of this

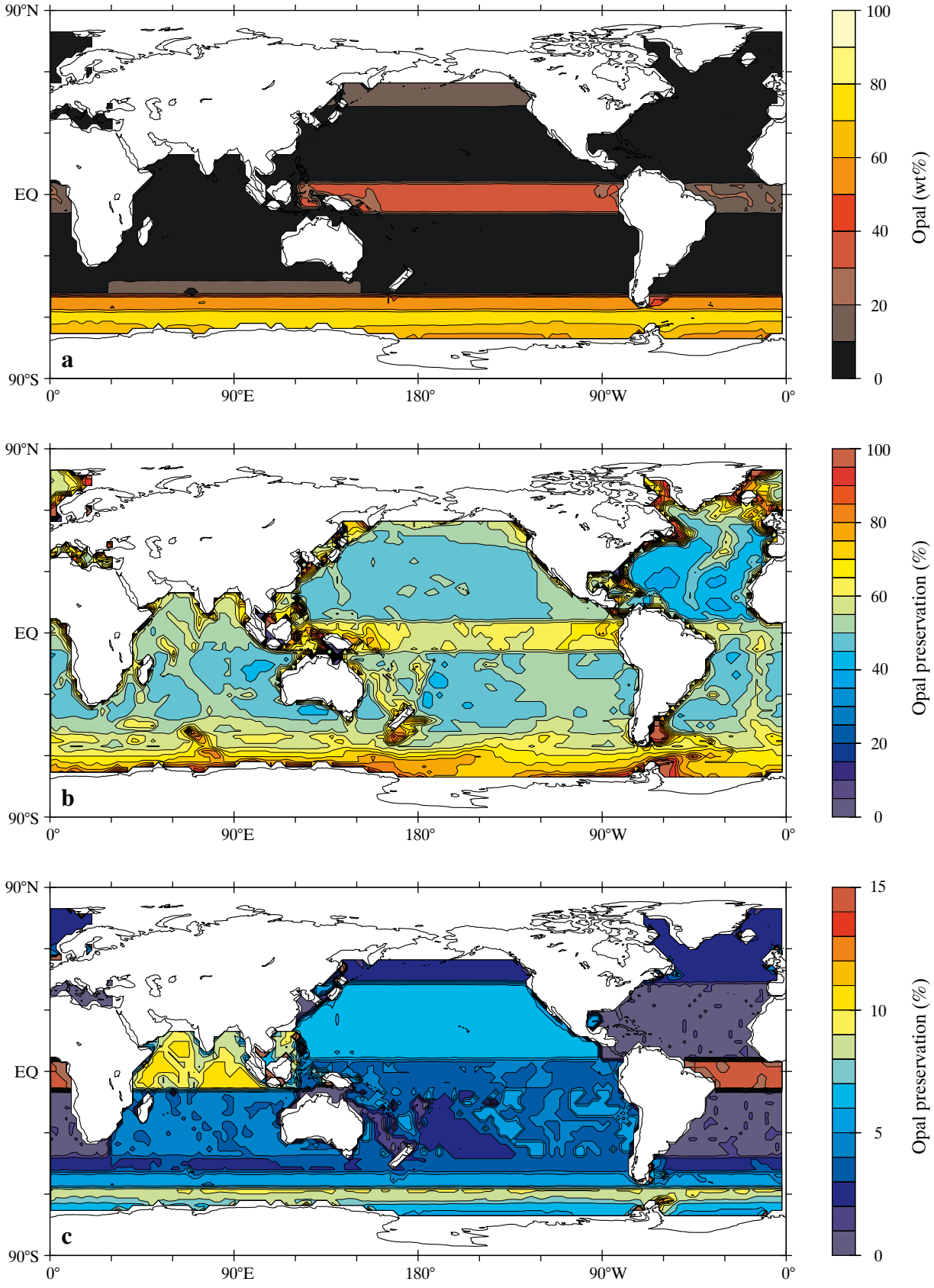

Figure 4-14 Modern steady-state distributions generated by SUE2108 of; (a) sediment surface wt% opal, (b) opal preservation efficiency within the water column, and (c) opal preservation efficiency within the sediments. Spatial resolution is gridded at 2.5°×2.5°.

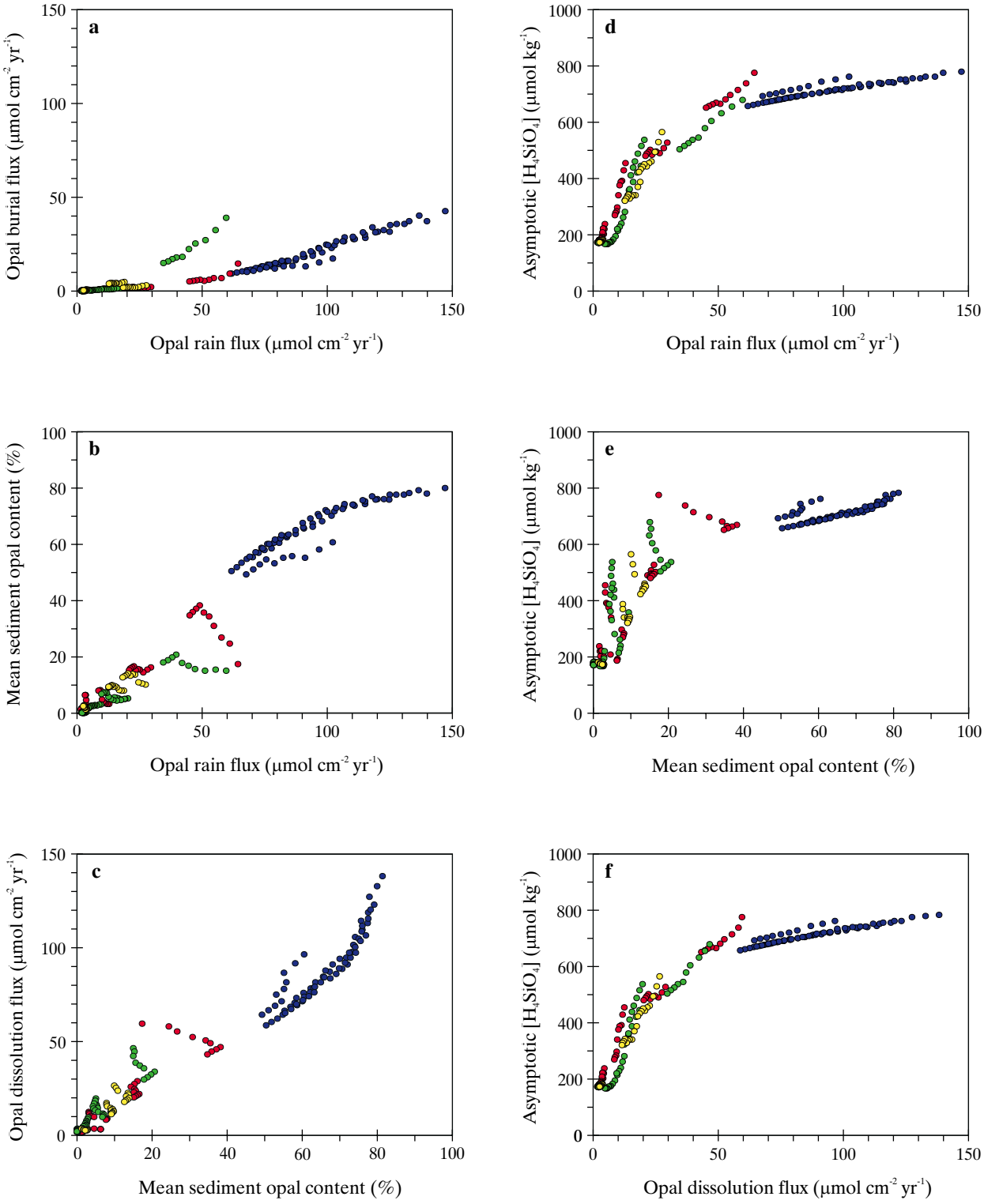

Figure 4-16 Combined response of the opal diagenesis model within SUE2108, shown by small filled circles colour-coded by ocean region; Southern Ocean (blue), Atlantic Ocean (green), Indian Ocean (yellow), Pacific Ocean (red). Sediments lying at depths shallower than 1000 m are excluded.

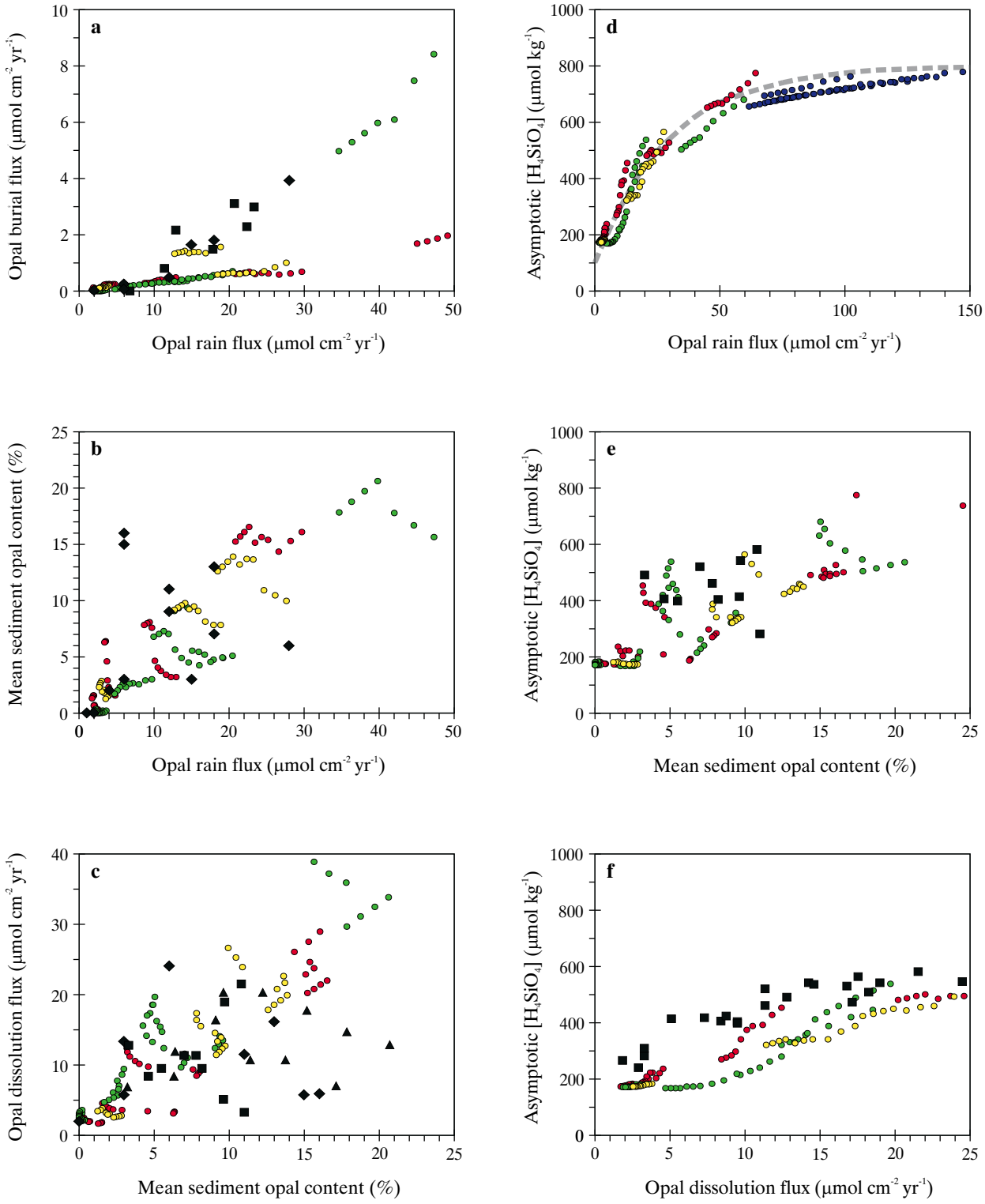

Figure 4-17 Combined response of the opal diagenesis model within SUE2108 shown by small filled circles colour-coded by ocean region; Southern Ocean (blue), Atlantic Ocean (green), Indian Ocean (yellow), Pacific Ocean (red). Sediments lying at depths shallower than 1000 m are excluded. Also shown is the validation data, indicated by larger filled symbols; squares - *McManus et al.* [1995], diamonds - *Archer et al.* [1993], triangles - *Martin et al.* [1991]. The thick dashed grey line in (d) indicates the estimated trend of *Archer et al.* [2000].

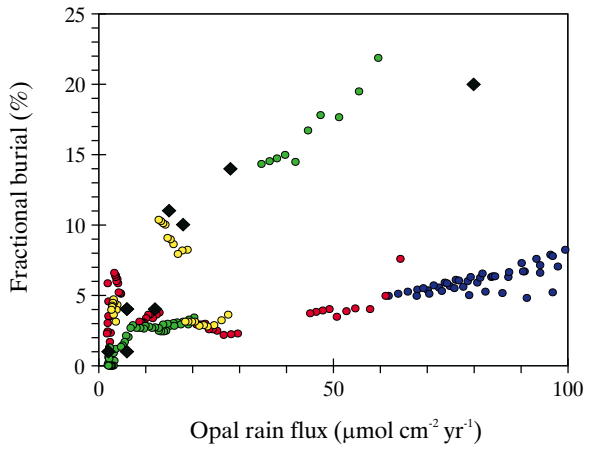

Figure 4-18 Combined response of the opal diagenesis model within SUE2108 shown by small filled circles colour-coded by ocean region; Southern Ocean (blue), Atlantic Ocean (green), Indian Ocean (yellow), Pacific Ocean (red). Sediments lying at depths shallower than 1000 m are excluded. Also shown is the validation data, indicated by larger filled diamonds [*Archer et al.*, 1993].

biogeochemically critical module is now carried out with SUE2108. Global functional (steady-state) relationships exhibited by the opal diagenesis module are displayed in Figure 4-16, with results from the four distinct ocean basins now differentiated. General trends are similar to before (3-11), although increased spatial resolution leads to trends being slightly better constrained with fewer prominent hiatuses. However, when model output is contrasted with the validation data set (Figure 4-17) the performance of the opal diagenesis module appears to be significantly better than suggested by the original analysis (3.2.3.5). Most striking is that the observed trend of opal burial flux with rain flux (a) is now extremely well reproduced whereas before, the slope was underestimated by a factor of >2. Interestingly, although the observational data delineating this trend is derived from cores mainly located in the eastern equatorial and temperate northeast Pacific [*Archer et al.*, 1993; *McManus et al.*, 1995], the matching model results come from equatorial Atlantic and Indian Ocean grid points. In the model both these regions are characterized by relatively high aeolian detrital fluxes to the sediments with low $CaCO_3$ contents. Such conditions are similar to those found at the core locations in the eastern and northeast Pacific [*Archer et al.*, 1993; *McManus et al.*, 1995]. Thus, while there is a poor geographical correspondence between model regions and core locations, there is a much close match on the basis of prevailing biogeochemical conditions (which the diagenesis module appears to be correctly responding to). Observed relationships between both opal content and asymptotic $[H_4SiO_4]$ with rain flux ((b) and (d), respectively), and also asymptotic $[H_4SiO_4]$ with opal content (e) are well reproduced as before. Although the observed trend of asymptotic $[H_4SiO_4]$ with dissolution flux (f) is slightly improved, it is obvious both from this and from the trends of dissolution flux with opal content (c) that dissolution fluxes are still somewhat over-predicted. Despite the continued existence of apparent deficiencies in several of the functional relationships characterizing opal diagenesis, behaviour critical to the global silica cycle such as the degree of fractional burial as a function of the flux of biogenic opal is still captured (Figure 4-18).

4.6 Summary

It is clear that significant deficiencies in the representation of global biogeochemical cycles arise out of zonalization of ocean circulation and structure. However, in spite of this SUE1608 is generally successful in capturing the characteristics of most of the key distinct biogeochemical provinces in the world ocean. Furthermore, SUE is designed to capture the dynamics of the carbon cycle on glacial-interglacial time scales, for which failure to accurately simulate the modern state is not necessarily a strict pre-requisite. Indeed, for long-term dynamical realism it is probably better to retain deficiencies arising from problems in the physical ocean representation rather than compensate for them by distorting biogeochemical cycling.